気液界面に生じる乱れと波崩れに関する研究

（研究課題番号　　０８４５５４７３）

平成８年度～平成９年度科学研究費補助金（基盤研究（Ｂ）(2)）研究成果報告書

平成１０年３月

研究代表者　　茂里　　一紘
（広島大学工学部教授）

気液界面に生じる乱れと波崩れに関する研究

（研究課題番号　　０８４５５４７３）

平成８年度～平成９年度科学研究費補助金（基盤研究（Ｂ）(2)）研究成果報告書

平成１０年３月

研究代表者　茂里　　一紘
（広島大学工学部教授）

はしがき

気液界面の非線形現象としての波崩れは、これまでに様々な分野で研究されてきた。近年の計測技術や数値流体力学の進歩により、波崩れに対する関心は一段と高まっており、波崩れの形態による分類もなされている。しかしながら、波崩れの現象は極めて複雑であり、そのメカニズムに対する明確な説明はなされていない。これまでの研究では、強い非線形現象である巻波が主な対象となっているが、当申請者らは、波崩れ発生初期の弱い非線形現象としての波崩れが乱流現象に近いことに着目して研究を始めた。その研究では、気液界面に存在する波流れが、ある遷移域を境に不安定になり、界面近傍で乱れた流れとなることを不安定解析や乱れの計測を行うことにより示している。

本研究ではこれらの背景をもとに、波崩れを気液界面における乱流現象と考え、波崩れ発生初期の現象に着目し、その前兆現象である渦流れの発生機構を数値シミュレーションにより明らかにする。さらに、波面に乱れを伴うsub-breaking waveの数値シミュレーションを行い、気液界面における乱れと波崩れ現象を明らかにする。

研究組織

研究代表者	：	茂里一紘	（広島大学工学部教授）
研究分担者	：	土井康明	（広島大学工学部助教授）
研究分担者	：	徐　埼	（広島大学工学部講師）
研究分担者	：	二宮伸治	（広島大学工学部助手）

研究経費

平成８年度	3、７００千円
平成９年度	1、６００千円
計	5、３００千円

研究発表

(1) 学会誌等

Yasuaki Doi, Uh-Cheul Jeong, Vorticity Generation on the Curved Free Surface around Bow Proceedings of CFD Symp. for Free-Surface Flows, pp.43-52 (1996)

Uh-Cheul Jeong, Yasuaki Doi, Numerical Study of Separated Flows on the Free Surface around Struts, The Third Korea-Japan Joint Workshop on Ship and Marine Hydrodynamics, pp.301-308 (1996)

Uh-Cheul Jeong, Yasuaki Doi, Kazu-hiro Mori, Turbulence on the Free Surface around Bow, Second Workshop on Hull Form Design & Flow Phenomena, pp.193-209 (1996)

Uh-Cheul Jeong, Yasuaki Doi, Kazu-hiro Mori, Numerical Investigation on the Turbulent and Vortical Flows beneath the Free Surface Around Struts Twenty-First Symposium on Naval Hydrodynamics, pp.794-809(1997)

Kazu-hiro Mori, Yasuaki Doi, Uh-Cheul Jeong, Tubulent Flow Simulation of Sub-Breaking Wave, Proceedings of the 1997 ASME Fluids Engineering Division,FEDSM97-3392(1997)

研究成果

本研究では波崩れ発生初期の現象に着目し、その前兆現象である渦流れの発生機構と波面に乱れを伴うsub-breaking waveを数値シミュレーションにより解析した。

第１章では、水面を貫通する物体の先端まわりの波崩れ現象に関する既往の研究を概説し、数値シミュレーションによる研究の必要性と本研究の背景を述べた。

第２章では、気液界面近傍に生じる渦流れに関する実験的知見について述べ、水面貫通柱状模型を用いて、気液界面流れの観察を行い、水面貫通物体の先端まわりに波面に乱れを伴うsub-breaking waveが存在することを示した。

第３章では、本研究で用いる流場の支配方程式ならびに境界条件を示し、その数値計算法について述べた。気液界面ではせん断力をゼロとする条件を課している。また、物体表面の乱流境界層と気液界面近傍にできる渦流れを判別するために、Baldwin-Lomaxモデルを改良した乱流モデルを導入した。

第４章では、数値計算法の精度について検討した。無限流中ならびに気液界面流れについて、数値計算で用いた時間および格子の違いによる結果を系統的に検討し、実験結果と比較することによって計算法の妥当性を検証した。

第５章では、２章で示した数値シミュレーション法を用いて、水面を貫通する物体の先端まわりの気液界面渦流れを検討した。気液界面上の力学的条件として

せん断力をゼロとする条件を課すことにより生じる渦度と波面の曲率について調査するとともに、水面貫通物体の先端まわりの気液界面渦流れの構造を明らかにし、これまで水波の数値シミュレーションに用いられてきた気液界面条件では気液界面の渦度を十分に計算できず、実際にはない急峻な波形を模擬することを示した。また、肥瘠度と水面貫通物体の先端まわりの渦流れの関連を示した。

５章の解析は気液界面が安定な状態に対するものであった。さらにフルード数を上げた状態では流れ場が不安定になりsub-breaking状態に遷移する。５章で用いた計算法ではこのような流れ場は計算できない。第６章では、sub-breaking waveを直接計算するためのLarge Eddy Simulationによる解法を示し、数値シミュレーションにより乱流場の構造を示すとともに実測と比較検討した。

第７章では、水面貫通物体の肩近傍の気液界面で発生する剥離流れの数値シミュレーションを行い、水面貫通物体の先端まわりに発生する渦流れとの関連を検討した。

以上のように、本研究は、水面貫通物体の先端まわりの流場解析を行うための計算法を開発し、数値シミュレーションにより気液界面渦流れと乱れの研究を行い、波崩れのメカニズム解明に重要な知見を与えた。

本研究では波崩れ発生初期の前兆現象である渦流れの発生機構と波面に乱れを伴うsub-breaking waveを数値シミュレーションにより解析した。今後、さらに乱れが発達した状態の解析とその抑制法を検討することが望まれる。

第1章 研究の背景

Baba[1] proposed wave breaking resistance as a new component of ship resistance. He could provide quantitative evidence of a resistance component due to wave breaking around the bow through measuring head-loss by wake survey method. Taneda and Amamoto[2] explained the bow breaking wave as a vortex motion. They called it "necklace vortex" to distinguish from the horseshoe vortex which was mainly generated by a boundary layer flow around a body mounted on a plate. They also reported that this necklace vortex was strongly affected by the Froude number while the horseshoe vortex was affected by the Reynolds number[2,3].

Since then, many investigations have been made to clarify the mechanism of the bow wave breaking both experimentally and numerically.

Experimental investigations

Experimental observations of the formation of bow vortical flows and the fluctuations of the free surface related to the bow breaking waves have been made, for example, by Miyata et al.[4-7], Grosenbaugh and Yeung[8], Kayo and Takekuma[9], Ogiwara et al.[10], Takekuma and Eggers[11], Matsui et al.[12] and so on. Miyata et al.[4-7] and Grosenbaugh and Yeung[8] showed an oscillatory motions of bow wave front which occurred when a certain critical speed was exceeded. Miyata et al.[6] also explained that overturning of waves generated a necklace vortex of which intensity depended on the strength of the overturning motion. Moreover, they reported that the vorticity generated by the breaking waves spreaded forward by the movement of wave front and backward by diffusive effect. However, it may be difficult to say that their findings are general characteristics of bow waves because they used two-dimensional floating bodies. Kayo and Takekuma[9] carried out a model test to explain the effect of a shear flow on the free surface. They towed a vinyl sheet in front of a bow with the same speed of a ship. They showed that the fluctuations of the free surface became intensive when a vinyl sheet was towed together. They deduced that the shear flow of the free surface had a significant effect on the formation of the bow breaking waves and vortical motions. Ogiwara et al.[10] reported that the vortical motions were mainly generated by the flow above a stagnation point on the body surface. On the other hand, Takekuma and Eggers[11] explained that the bow wave breaking was characterized by the vortical motions below the free surface. The vortical motions located just below the free surface where the flow broke and the region of the vortical motions did not extend widely and the depth was nearly as deep as the wave height. They also showed that the intensity of the vortical motions around the body in a shallower draft was stronger than that in a deeper draft. Matsui et al.[12] performed a series of model tests to find out the effect of the draft and bow curvature on the vortical motions. They investigated the relation between the bow curvature and the distance from the bow to wave front at the center plane. However, the relation could not be made clearly. The reason may be that the position of the wave front is not so clear at a low speed. On the other hand, it is difficult to measure the position at a high

speed region because the position may fluctuate or oscillate above a certain velocity.

All the studies mentioned above are mainly concerned to the "broken" waves. However, to make clear the phenomena it may be necessary to study the earlier stage where the breaking is apt to occur.

Kayo and Takekuma[11] and Honji[13] experimentally showed the vortical motion beneath the free surface around the bow at a very low Froude number where no significant bow waves were generated. They explained that these results might be caused by the shear flow on the free surface.

On the other hand, Mori[14,15] divided the flow into three stage; the development of the free surface shear layer, the formation of the necklace vortex and the production of unsteady turbulent free surface flow. The final stage was called "sub-breaking waves" as a free surface turbulent flow in distinction from spilling or plunging breakers. He showed the characteristics of the sub-breaking waves by measuring the velocity components around the first wave crest generated by a two-dimensional submerged hydrofoil[14]. His experimental results have shown that when the velocity is less than the critical value, the wave crests remain rounded and no symptoms of breakings are present but once the velocity increases even a little beyond the critical one, the steady breakers suddenly takes place. The wave amplitude under the sub-breaking becomes smaller while the wave length shorter as if Froude number were smaller. If the oncoming flow is further accelerated, this intermediate stage is overcome by the breakers such as spilling or overturning. He explained that the sub-breaking waves could be understood as follows; the energy accumulated around the wave crest transits into the turbulent flow to meet the required free surface condition. The energy of the main stream is transformed into a turbulent energy which dissipates at the same time. Eventually main stream has velocity defects, i.e. head-loss, and the flow remains without any catastrophic breakings. He also investigated the curvature effect of the bow using a circular cylinder and an elliptic strut[15]. According to his experimental results, the bow with a larger curvature (elliptic strut) generated more intensive wrinkle, which was a kind of free surface instability, than that generated by the bow with a smaller one(circular cylinder) at the same speed. He explained that the reason was the different curvature of the free surface in front of the bows.

Numerical investigations

Recently, the CFD(Computational Fluid Dynamics) becomes a general tool in various scientific fields; aeronautics, mechanical engineering, civil engineering, naval architecture and ocean engineering and so on. A main merit of the CFD technique is that it makes possible to study the complicated phenomena systematically when the experimental investigations are difficult. In the field of ship hydrodynamics, many attempts have been made to simulate the flow around ship[16-18]. However, there are some difficulties to simulate the free surface flow especially bow and shoulder wave breakings. The difficulties are mainly caused by the free surface boundary condition under the breaking condition because the mechanism of the breaking waves have not yet come to knowledge clearly.

Miyata et al.[19] explained that at a high Froude number, steep waves generated alongside of the bow

were nondispersive and they call them "free-surface shock waves(FSSW)". Duncan[20] found that it was possible to introduce steady breaking by disturbing non-breaking wave-train which was a transition from a non-breaking to a breaking waves although within a narrow range. Shin and Mori[21,22] simulated the sub-breaking wave generated by two-dimensional submerged hydrofoil. They introduced the Reynolds stress components on the free surface boundary condition which were modeled by the measured velocity on the free surface. They suggested that the turbulence terms played an important role in the computations of the sub-breaking waves. Hinatsu and Takeshi[23] also simulated breaking waves in front of a two-dimensional box-shaped body. As a first step for the simulations, they measured the velocity components in front of the body by LDV system. Then they modeled the turbulent shear stress on the free surface. Their results gave one possibility for the direct simulation of the breaking waves although the results did not agree well with the experimental results. Lungu and Mori[24,25] simulated two-dimensional sub-breaking waves directly by imposing a disturbance for vertical velocity component while Coleman[26] used a disturbance of pressure on the free surface. The role of these disturbances was a kind of a trigger for the transition to the turbulent flow. Shin et al.[27], Park and Miyata[28] also studied the characteristics of the bow breaking waves by numerical simulation method. However they did not consider the viscous effect on the free surface although the viscous effect was important to that kind of the flows as pointed out by Patel et al.[29] who simulated the vortical flows under the similar condition with the Honji's experiment[13] as mentioned before. They theoretically explained that the vortical flows at a low Froude number could be caused by the balance of a surface tension and a normal component of a viscous stress. Yeung and Ananthakrishnan[30] simulated the vortical flows in front of the two-dimensional rectangular body. They explained that the surface tension was important and the vorticity strength due to the free surface curvature was not so strong. However, Jeong et al.[31,32] suggested that the free surface curvature could be one of the important sources of the vortical flows beneath the free surface around a blunt bow.

As investigated above, the so-called bow breaking waves and necklace vortex motion are not so simple and the mechanism has not yet come to knowledge clearly. Further studies are required to clarify the mechanism.

第2章　気液界面渦流れの観察

In this chapter, some experimental results concerning vortical flows around bow are discussed to understand the basic characteristics of the vortical flows.

1 Review of Experimental Investigations

According to some experimental results, vortical flows exist beneath the free surface in front of a blunt bow. Fig.2.1 shows a schematic view of the vortical flows by Taneda et al.[3]. They explained that the flow patterns on the free surface around a surface piercing body were similar with a horseshoe vortex which appeared around a strut mounted on a plat(Fig.2.2). They called it "necklace vortex" to distinguish from the horseshoe vortex. They deduced that the necklace vortex was strongly affected by the Froude number while the horseshoe vortex was affected by the Reynolds number. Fig.2.3 shows a sketch of a generation of the vortical flows by Miyata et al.[6]. They explained that overturning of waves generated a necklace vortex of which intensity depended on the strength of the overturning motion. Moreover, they reported that the vorticity generated by the breaking waves spreaded forward by the movement of wave front and backward by diffusive effect.

However, Takekuma et al.[11] and Honji[13] showed the existence of the vortical flows beneath the free surface even a extremely low Froude number(Figs.2.4-2.5). However, the characteristics seem to be different from those observed in the breaking wave. As shown in Figs.2.4 and 2.5, the free surface is almost flat and no significant bow waves are observed. The strength of the vortical motion is very weak. They deduced that the vortical flows were caused by the shear flow on the free surface while Patel et al.[29] theoretically explained that the vortical flows at a low Froude number could be caused by the balance of a surface tension and a normal component of a viscous stress.

The effect of shear flow on the bow breaking waves was also investigated by Kayo and Takekuma[9]. They towed a vinyl sheet in front of a bow with the same speed of a ship. They showed that the fluctuations of the free surface became intensive when the vinyl sheet was towed together(Fig.2.6).

Fig.2.7 shows the typical free surface flows around a circular cylinder at various draft by Takekuma and Eggers[11]. As shown, the free surface flows in front of the bow are more intensive in shallower draft than in deeper draft. Fig.2.8 shows the vortical flows beneath the free surface in front of the bow on the center plane for two different draft. The vortical flows in shallower draft are more intensive than those in deeper draft. This can explain the reason why bow wave breaking in ballast condition is more intensive than in full load condition. They also investigated the effect of a underwater protruding bulb on the vortical flows. As shown in Fig.2.9, the vortical flows become weak in case that the bulb is attached. This can explain that a well-designed bulbous bow can play an important role to reduce the vortical flows.

On the other hand, Mori[15] investigated the curvature effect of the bow using a circular cylinder and an

elliptic strut(Fig.2.10). As shown in this figure, the bow with a larger curvature (elliptic strut) generated more intensive wrinkle, which was a kind of free surface instability, than that generated by the bow with a smaller one(circular cylinder) at the same speed. He explained that the reason might be the different curvature of the free surface in front of the bows. The effect of bow curvature will be discussed in the next section continuously.

2 Observation of Bow Wave Patterns

In the present study, an observation of bow wave patterns was performed for the struts having NACA0008, NACA0012 and NACA0024 sections(called NS08, NS12 and NS24 hereafter) at the circulating water channel(CWC) of Hiroshima University. The length and the draft of the models were 0.8m and 0.4m respectively. Experimental arrangement is shown in Fig.2.11. The wave patterns were photographed through the observation window placed on the bottom of the CWC. The striped-screen was fixed above the free surface to make the pictures clear. The pictures were taken with a surfactant, which was a commercial detergent, to remove a surface tension[33].

Fig.2.12 shows a sketch of the bow wave on the center plane. The "Zone-I" where the free surface has smooth concave curvature is the part ahead of the bow wave. Through a sharp change of the curvature, the flow enters "Zone-II" where the flow can not be stable any more. A border of these two zones is "wave front" where the curvature has a maximum[15].

Fig.2.13 shows the flow patterns on the free surface around the bow of NS12 at various Froude numbers. No clear waves are observed at Fn=0.15(Fig.2.13(a)). Increasing the Froude number(Fn=0.20), the wave front can be clearly observed surrounding the bow(Fig.2.13(b)). At Fn=0.25, the wave front appears clearly and the position moves away from the bow(Fig.2.13(c)). At those Froude numbers, no significant features of turbulence appear on the free surface.

Fig.2.14 shows the free surface flows around the bows at Fn=0.30 for the three models. The Reynolds number based on the length of the strut is 4.60×10^5. The free surface flows of NS08 and NS12 seem to be quite complicated and turbulent in "Zone-II" which can be called the sub-breaking wave[14,15]. The wrinkles of NS08 and NS12 are more intensive than NS24 around the bow. However, the flow of NS24 looks still gentle. Here, a question may appear; why the intensity of the free surface wrinkles of NS08 is much stronger than that of NS24 although the bow of NS24 is much blunter? Similar results were obtained by Mori[15] as shown in Fig.2.10. The detail discussions on the effect of bow curvature will be made by a numerical simulation in Chapter 5.

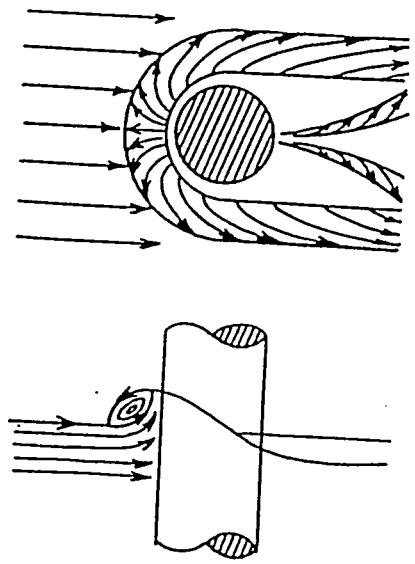

Fig.2.1 Schematic view of necklace vortex and vortical motions on the free surface around circular cylinder, Taneda et al.[3].

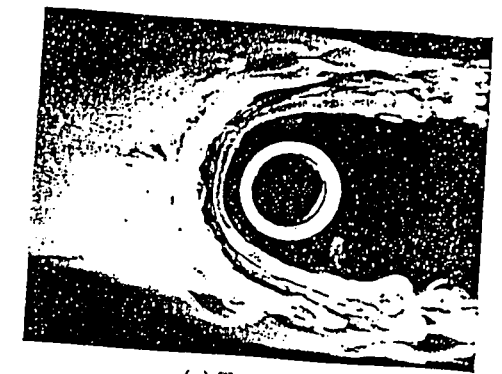

(a) Top view

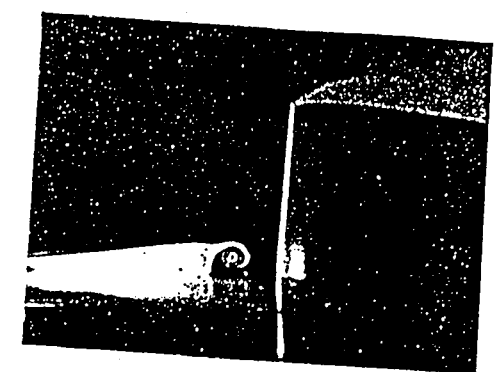

(b) Side view

Fig.2.2 Pictures of horseshoe vortex, Taneda et al.[3].

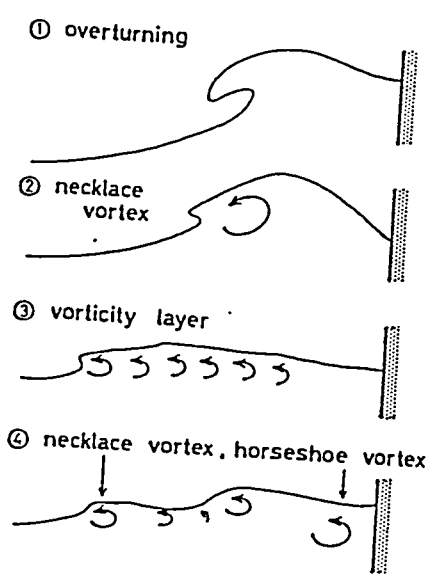

Fig.2.3 Sketch of vortex generation in bow wave, Miyata et al.[6].

(U=0.05 m/s, D=0.45 m)

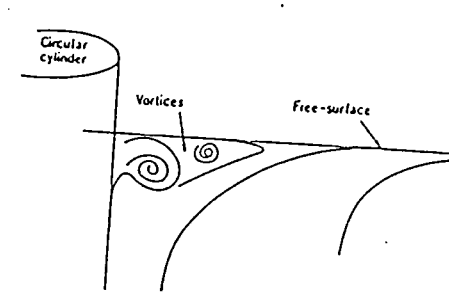

Fig.2.4 Vortical flows beneath free surface in front of circular cylinder (Body moves from left to right), Takakuma et al.[11].

(U=0.039 m/s, D=0.10 m)

Fig.2.5 Vortical flows beneath free surface in front of two-dimensional horizontal circular cylinder(Body moves from right to left), Honji[13].

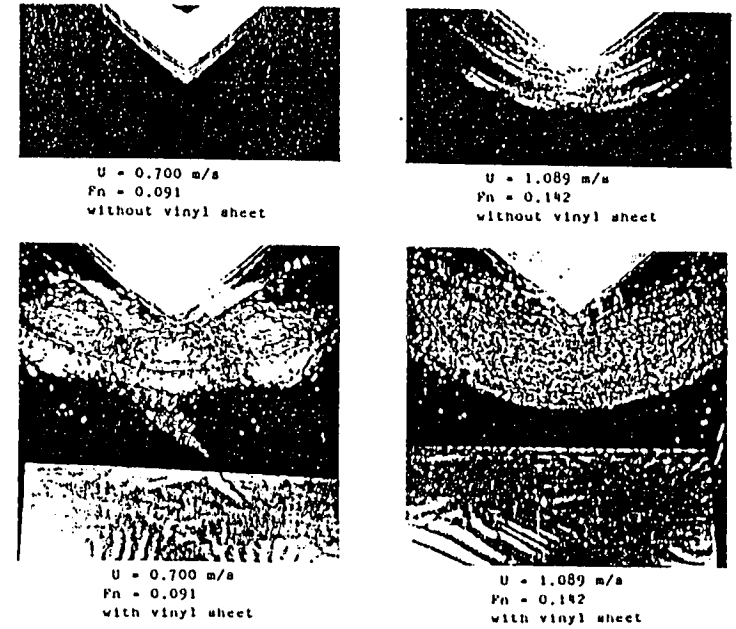

Fig.2.6 Effect of shear flow on free surface in front of bow, Kayo et al.[9].

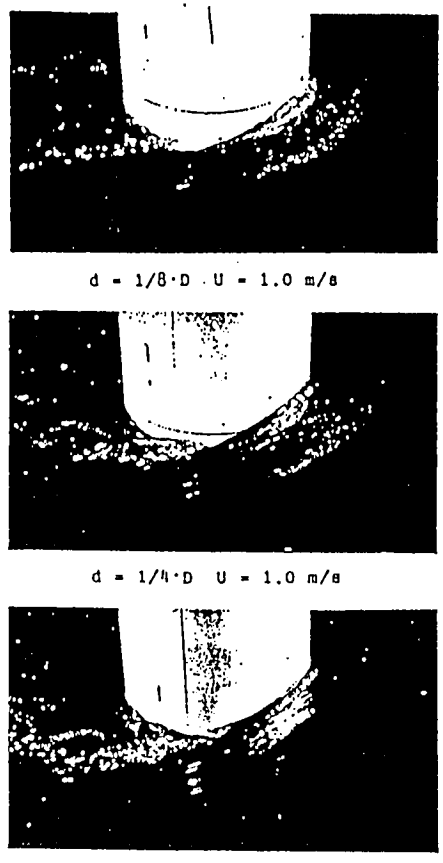

Fig.2.7 Draft effect on bow waves of circular cylinder (D=0.45 m, Bodies move from left to right), Takekuma et al.[11].

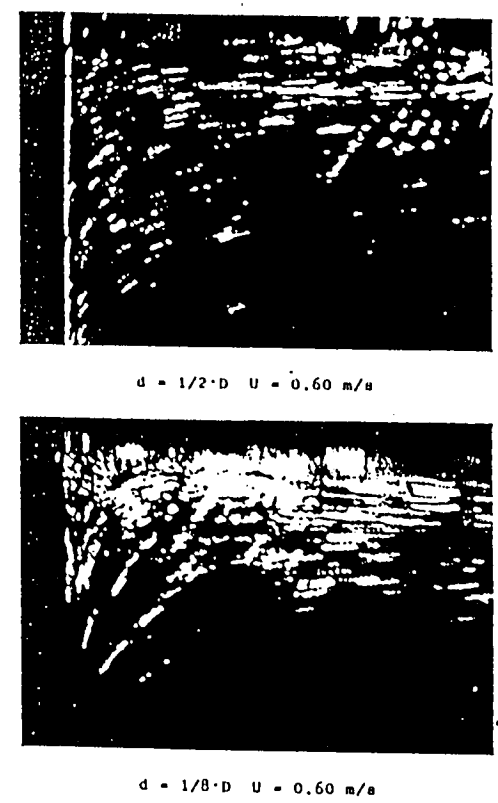

Fig.2.8 Draft effect on vortical flows at center plane in front of circular cylinder(R=0.45 m, Bodies move from left to right), Takekuma et al.[11].

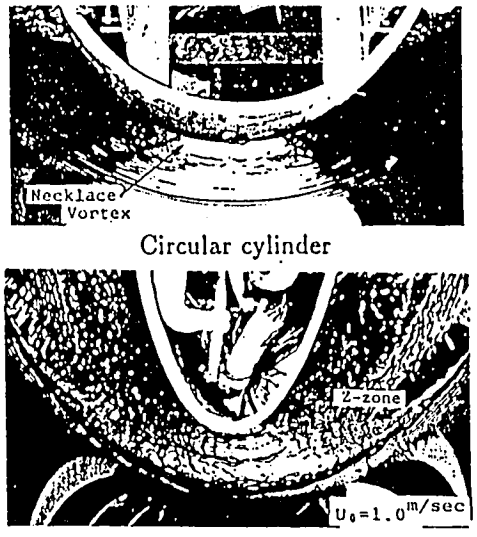

Fig.2.10 Curvature effect on bow wave(U=1.0 m/s), Mori[15].

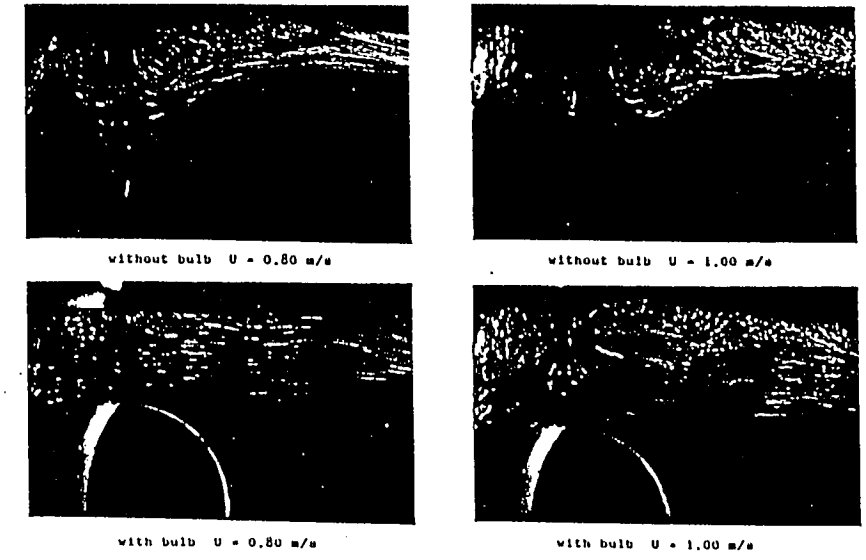

Fig.2.9 Bulb effect on vortical flows in front of circular cylinder (D=0.45 m, Bodies move from left to right), Takekuma et al.[11].

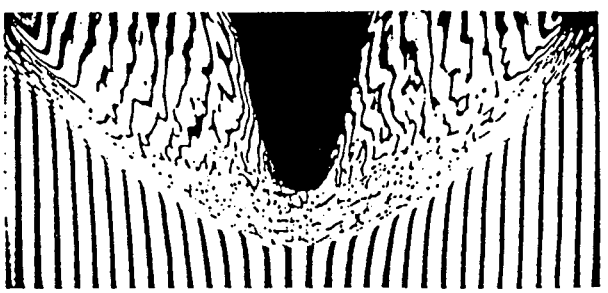

(a) NS08

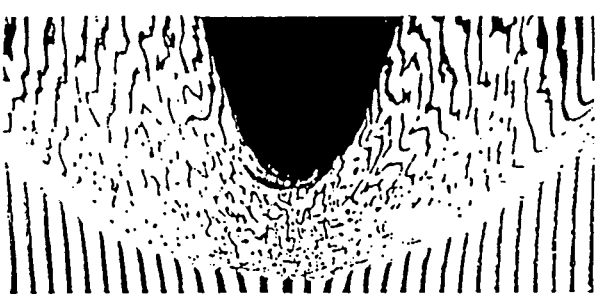

(b) NS12

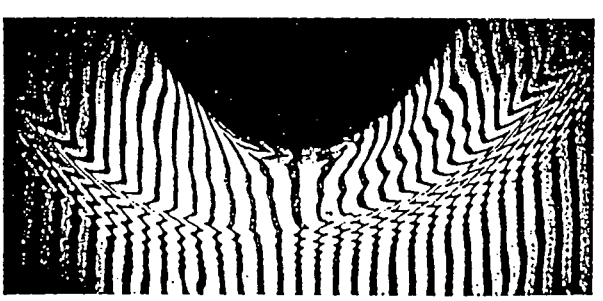

(c) NS24

Fig.2.14 Free surface flows around bows of NS08, NS12 and NS24, U=0.84 m/s, Fn=0.30, Rn=4.6 · 10^5.

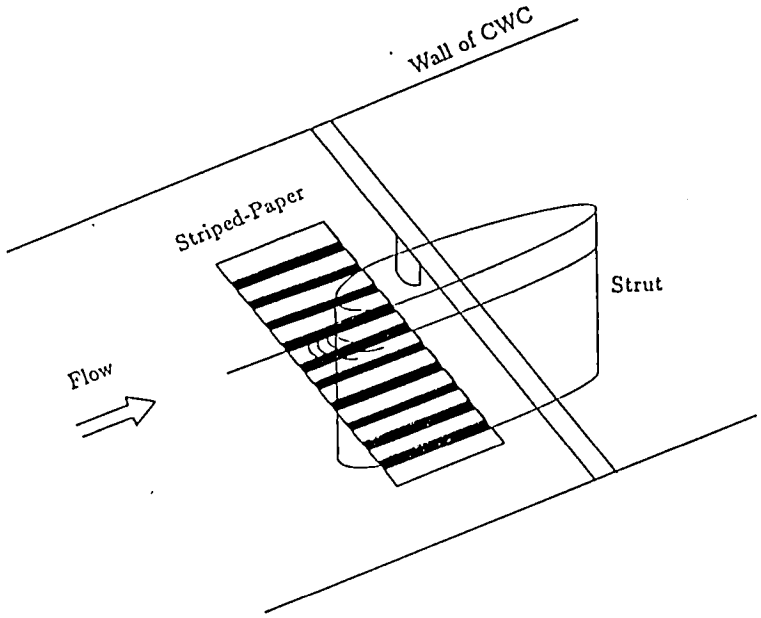

Fig.2.11 Experimental set-up for observation of free surface flows in CWC.

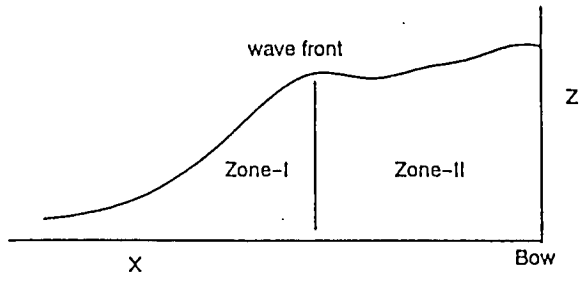

Fig.2.12 Schematic view of bow wave.

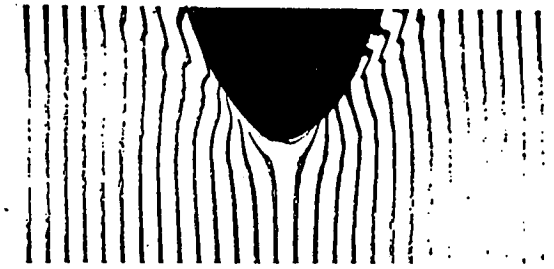

(a) U=0.42m/s, Fn=0.15, Rn=2.3·10^5

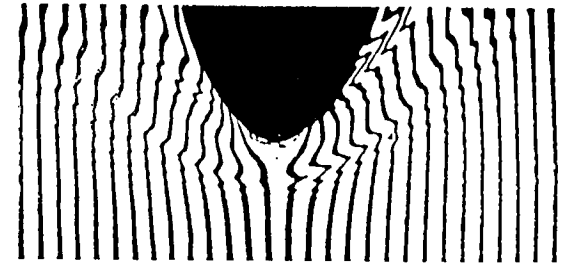

(b) U=0.56m/s, Fn=0.20, Rn=3.1·10^5

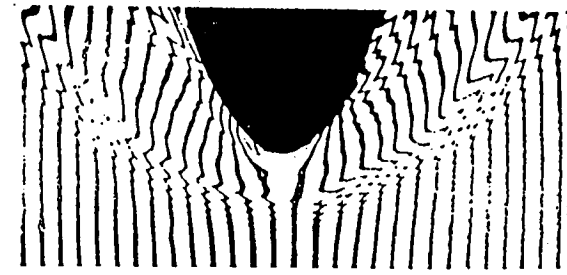

(c) U=0.78m/s, Fn=0.25, Rn=3.9·10^5

Fig.2.13 Free surface flows around bow of NS12 at various speed.

第3章　気液界面流れの数値計算法

1 Governing Equations

Three dimensional incompressible time averaged Navier-Stokes(Reynolds averaged Navier-Stokes;RaNS) and continuity equations are employed for the present numerical study. These governing equations are written as follows;

$$u_t + uu_x + vu_y + wu_z = -\phi_x + \frac{1}{Rn}\nabla^2 u + R_x$$

$$v_t + uv_x + vv_y + wv_z = -\phi_y + \frac{1}{Rn}\nabla^2 v + R_y \tag{1}$$

$$w_t + uw_x + vw_y + ww_z = -\phi_z + \frac{1}{Rn}\nabla^2 w + R_z$$

$$u_x + v_y + w_z = 0 \tag{2}$$

$$\phi = p + \frac{z}{Fn^2} - P_{at} + \frac{2}{3}k \tag{3}$$

where u, v and w are the velocity components in (x,y,z)-directions in the Cartesian co-ordinate system as shown in Fig.3.1; x in the uniform flow, y in the lateral and z in the vertical directions respectively. The origin is located at the leading edge of the strut on the undisturbed free surface. Subscripts represent partial differentiations with respect to the referred variables except R_x, R_y and R_z which are Reynolds stress components. Fn, Rn, ϕ, p, P_{at} and k are Froude number, Reynolds number, modified pressure, pressure, atmospheric pressure and turbulent energy respectively. All the variables are normalized by the uniform velocity(U_0) and the length of strut(L).

The Reynolds stress terms can be expressed as follows;

$$R_x = \{\nu_t(u_x + u_x)\}_x + \{\nu_t(u_y + v_x)\}_y + \{\nu_t(u_z + w_x)\}_z$$

$$R_y = \{\nu_t(u_y + v_x)\}_x + \{\nu_t(v_y + v_y)\}_y + \{\nu_t(v_z + w_y)\}_z \tag{4}$$

$$R_z = \{\nu_t(u_z + w_x)\}_x + \{\nu_t(v_z + w_y)\}_y + \{\nu_t(w_z + w_z)\}_z$$

where ν_t represents kinematic eddy viscosity.

2 Co-ordinate Transformation

A numerical co-ordinate transformation is introduced into a body fitted curvilinear co-ordinate system to simplify the computational domain and to facilitate the implementation of boundary conditions.

A half C-H type grid system is used to simulate the flow around a blunt bow while a half H-H type one is used for a wedge shaped model. The curvilinear co-ordinate system on horizontal plane is shown in Fig.3.1; ξ- and η-axes are the streamwise and lateral directions respectively and ζ-axis coincides with the z-axis.

The transformation is given as follows;

$$\xi = \xi(x, y, z, t)$$

$$\eta = \eta(x, y, z, t) \tag{5}$$

$$\zeta = \zeta(x, y, z, t)$$

$$\tau = t.$$

The transformation links the partial derivatives expressed on the physical and computational domains through the following formula.

$$\frac{\partial}{\partial x} = \xi_x \frac{\partial}{\partial \xi} + \eta_x \frac{\partial}{\partial \eta} + \zeta_x \frac{\partial}{\partial \zeta}$$

$$\frac{\partial}{\partial y} = \xi_y \frac{\partial}{\partial \xi} + \eta_y \frac{\partial}{\partial \eta} + \zeta_y \frac{\partial}{\partial \zeta} \tag{6}$$

$$\frac{\partial}{\partial z} = \xi_z \frac{\partial}{\partial \xi} + \eta_z \frac{\partial}{\partial \eta} + \zeta_z \frac{\partial}{\partial \zeta}$$

$$\frac{\partial}{\partial t} = \frac{\partial}{\partial \tau} - x_t \frac{\partial}{\partial x} - y_t \frac{\partial}{\partial y} - z_t \frac{\partial}{\partial z}$$

With the above relations, the following transformed governing equations are obtained.

- RaNS equations

$$u_\tau = F - \phi_x$$

$$v_\tau = G - \phi_y \tag{7}$$

$$w_\tau = H - \phi_z$$

$$\phi_x = \phi_\xi \xi_x + \phi_\eta \eta_x + \phi_\zeta \zeta_x$$

$$\phi_y = \phi_\xi \xi_y + \phi_\eta \eta_y + \phi_\zeta \zeta_y \tag{8}$$

$$\phi_z = \phi_\xi \xi_z + \phi_\eta \eta_z + \phi_\zeta \zeta_z$$

where,

$$F = -(Uu_\xi + Vu_\eta + Wu_\zeta) + \frac{1}{Rn}\nabla^2 u + R_x + f$$

$$G = -(Uv_\xi + Vv_\eta + Wv_\zeta) + \frac{1}{Rn}\nabla^2 v + R_y + g \tag{9}$$

$$H = -(Uw_\xi + Vw_\eta + Ww_\zeta) + \frac{1}{Rn}\nabla^2 w + R_z + h$$

$$f = u_x x_\tau + u_y y_\tau + u_z z_\tau$$

$$g = v_x x_\tau + v_y y_\tau + v_z z_\tau \tag{10}$$

$$h = w_x x_\tau + w_y y_\tau + w_z z_\tau$$

where, U, V and W are contravariant velocity components defined as

$$U = u\xi_x + v\xi_y + w\xi_z$$

$$V = u\eta_x + v\eta_y + w\eta_z \tag{11}$$

$$W = u\zeta_x + v\zeta_y + w\zeta_z$$

- Continuity equation

$$(u_\xi \xi_x + u_\eta \eta_x + u_\zeta \zeta_x) + (v_\xi \xi_x + v_\eta \eta_x + v_\zeta \zeta_x) + (w_\xi \xi_x + w_\eta \eta_x + w_\zeta \zeta_x) = 0 \tag{12}$$

Laplacian ∇^2 in F, G and H of equation(3.9) can be expressed in the curvilinear co-ordinate system as follows;

$$\nabla^2 q = (\hat{a} q_{\xi\xi} + \hat{b} q_{\eta\eta} + \hat{c} q_{\zeta\zeta}) + 2(\hat{d} q_{\xi\eta} + \hat{e} q_{\eta\zeta} + \hat{f} q_{\zeta\xi}) + (\hat{g} q_\xi + \hat{h} q_\eta + \hat{i} q_\zeta) \tag{13}$$

where $\hat{a}$, $\hat{b}$, etc. are defined as

$$\begin{aligned}
\hat{a} &= \nabla\xi \cdot \nabla\xi = \xi_x^2 + \xi_y^2 + \xi_z^2 \\
\hat{b} &= \nabla\eta \cdot \nabla\eta = \eta_x^2 + \eta_y^2 + \eta_z^2 \\
\hat{c} &= \nabla\zeta \cdot \nabla\zeta = \zeta_x^2 + \zeta_y^2 + \zeta_z^2 \\
\hat{d} &= \nabla\xi \cdot \nabla\eta = \xi_x\eta_x + \xi_y\eta_y + \xi_z\eta_z \\
\hat{e} &= \nabla\eta \cdot \nabla\zeta = \eta_x\zeta_x + \eta_y\zeta_y + \eta_z\zeta_z \\
\hat{f} &= \nabla\zeta \cdot \nabla\xi = \zeta_x\xi_x + \zeta_y\xi_y + \zeta_z\xi_z \\
\hat{g} &= \nabla^2\xi = \xi_{xx} + \xi_{yy} + \xi_{zz} \\
\hat{h} &= \nabla^2\eta = \eta_{xx} + \eta_{yy} + \eta_{zz} \\
\hat{i} &= \nabla^2\zeta = \zeta_{xx} + \zeta_{yy} + \zeta_{zz}
\end{aligned} \tag{14}$$

The second derivative terms $\hat{g}$, $\hat{h}$ and $\hat{i}$ in equation(3.14) are computed by the following formula.

$$\begin{aligned}
\hat{g} &= \nabla^2\xi \\
&= -\hat{a}(\xi_x x_{\xi\xi} + \xi_y y_{\xi\xi} + \xi_z z_{\xi\xi}) - \hat{b}(\xi_x x_{\eta\eta} + \xi_y y_{\eta\eta} + \xi_z z_{\eta\eta}) \\
&\quad -\hat{c}(\xi_x x_{\zeta\zeta} + \xi_y y_{\zeta\zeta} + \xi_z z_{\zeta\zeta}) - 2\hat{d}(\xi_x x_{\xi\eta} + \xi_y y_{\xi\eta} + \xi_z z_{\xi\eta}) \\
&\quad -2\hat{e}(\xi_x x_{\zeta\xi} + \xi_y y_{\zeta\xi} + \xi_z z_{\zeta\xi}) - 2\hat{f}(\xi_x x_{\eta\zeta} + \xi_y y_{\eta\zeta} + \xi_z z_{\eta\zeta}) \\
\hat{h} &= \nabla^2\eta \\
&= -\hat{a}(\eta_x x_{\xi\xi} + \eta_y y_{\xi\xi} + \eta_z z_{\xi\xi}) - \hat{b}(\eta_x x_{\eta\eta} + \eta_y y_{\eta\eta} + \eta_z z_{\eta\eta}) \\
&\quad -\hat{c}(\eta_x x_{\zeta\zeta} + \eta_y y_{\zeta\zeta} + \eta_z z_{\zeta\zeta}) - 2\hat{d}(\eta_x x_{\xi\eta} + \eta_y y_{\xi\eta} + \eta_z z_{\xi\eta}) \\
&\quad -2\hat{e}(\eta_x x_{\zeta\xi} + \eta_y y_{\zeta\xi} + \eta_z z_{\zeta\xi}) - 2\hat{f}(\eta_x x_{\eta\zeta} + \eta_y y_{\eta\zeta} + \eta_z z_{\eta\zeta}) \\
\hat{i} &= \nabla^2\zeta \\
&= -\hat{a}(\zeta_x x_{\xi\xi} + \zeta_y y_{\xi\xi} + \zeta_z z_{\xi\xi}) - \hat{b}(\zeta_x x_{\eta\eta} + \zeta_y y_{\eta\eta} + \zeta_z z_{\eta\eta}) \\
&\quad -\hat{c}(\zeta_x x_{\zeta\zeta} + \zeta_y y_{\zeta\zeta} + \zeta_z z_{\zeta\zeta}) - 2\hat{d}(\zeta_x x_{\xi\eta} + \zeta_y y_{\xi\eta} + \zeta_z z_{\xi\eta}) \\
&\quad -2\hat{e}(\zeta_x x_{\zeta\xi} + \zeta_y y_{\zeta\xi} + \zeta_z z_{\zeta\xi}) - 2\hat{f}(\zeta_x x_{\eta\zeta} + \zeta_y y_{\eta\zeta} + \zeta_z z_{\eta\zeta})
\end{aligned} \tag{15}$$

The metrics of the grid $(\xi_x, \xi_y, \xi_z, \ldots)$ are computed by the following relations.

$$\begin{aligned}
&\xi_x = (y_\eta z_\zeta - y_\zeta z_\eta)/J, \quad \eta_x = (y_\zeta z_\xi - y_\xi z_\zeta)/J, \quad \zeta_x = (y_\xi z_\eta - y_\eta z_\xi)/J \\
&\xi_y = (z_\eta x_\zeta - z_\zeta x_\eta)/J, \quad \eta_y = (z_\zeta x_\xi - z_\xi x_\zeta)/J, \quad \zeta_y = (z_\xi x_\eta - z_\eta x_\xi)/J \\
&\xi_z = (x_\eta y_\zeta - x_\zeta y_\eta)/J, \quad \eta_z = (x_\zeta y_\xi - x_\xi y_\zeta)/J, \quad \zeta_z = (x_\xi y_\eta - x_\eta y_\xi)/J
\end{aligned} \tag{16}$$

where, J is the Jacobian given by

$$J = \begin{vmatrix} x_\xi & x_\eta & x_\zeta \\ y_\xi & y_\eta & y_\zeta \\ z_\xi & z_\eta & z_\zeta \end{vmatrix} \tag{17}$$

3 Numerical Algorithm

MAC(Marker-and-Cell) type algorithm[34] is used in the present numerical study. By taking a divergence of the momentum equations and substituting the results into the continuity equation, the following Poisson equation for the pressure is obtained.

$$\nabla^2\phi = F_x + G_y + H_z - D_t \tag{18}$$

where F, G and H are defined in equation(3.9) and D is

$$D = u_x + v_y + w_z \tag{19}$$

The Poisson equation(3.18) is solved in place of the continuity equation imposing the divergence of $(n+1)$th time step(D^{n+1}) to be zero. Thus, D_t in equation(3.18) is expressed as follow by the first order Euler explicit scheme.

$$D_t = \frac{D^{n+1} - D^n}{\Delta t} = -\frac{D^n}{\Delta t} \tag{20}$$

where Δt denotes time increment and superscripts denote time step. Here, D^n is retained to prevent instability coming from the accumulation of numerical errors[35]. Thus, if a converged solution for the pressure is obtained the continuity is implicitly satisfied. The Poisson equation for the pressure is iteratively solved by using SOR(Successive Over Relaxation) method in the folllowing way.

$$\phi^{k+1} = \phi^k + \omega(\phi_o^{k+1} - \phi^k) \tag{21}$$

where ω represents the relaxation factor and superscripts indicate the number of iteration. ϕ_o^{k+1} is the most recent value calculated from the Liebmann procedure and ϕ^k is the value from the previous iteration. Iterations are stopped when the pressure difference between two consecutive approximations is smaller than a certain quantity, ϵ, chosen a priori.

After solving the pressure, the velocity components can be obtained from the momentum equations(3.7) by the first order upwind scheme as follows;

$$u^{n+1} = u^n + (F - \phi_x)\Delta t$$

$$v^{n+1} = v^n + (G - \phi_y)\Delta t \tag{22}$$

$$w^{n+1} = w^n + (H - \phi_z)\Delta t$$

where F, G and H are given in equation(3.9).

A finite difference method is represented on a regular grid system. So all the variables are defined on the grid nodes. The first order differencing of the time derivatives in NS equations is used for an explicit advancement in time. The convective terms in NS equations are discretized by the third order upwind scheme while the first order upwind scheme is used on the boundaries as follows in case that the grid spacing is the same.

- 1st order upwind scheme

$$U\frac{\partial u}{\partial \xi} = \frac{U_i}{2\Delta\xi}(u_{i+1} - u_{i-1}) - \alpha\frac{|U_i|}{2\Delta\xi}(u_{i+1} - 2u_i + u_{i-1}) \tag{23}$$

- 3rd order upwind scheme

$$\begin{aligned} U\frac{\partial u}{\partial \xi} &= \frac{U_i}{12\Delta\xi}(u_{i-2} - 8u_{i-1} + 8u_{i+1} - u_{i+2}) \\ &\quad + \alpha\frac{|U_i|}{4\Delta\xi}(u_{i-2} - 4u_{i-1} + 6u_i - 4u_{i+1} + u_{i+2}) \end{aligned} \tag{24}$$

where $\alpha = 1.0$ is used as a standard coefficient.
All the other spatial derivatives are discretized by the second order central differencing scheme except the boundary points while a oneside differencing scheme is introduced on the boundaries.

The computation starts from a rest condition and the flow is accelerated up to given velocity for the numerical stability. The effect of the acceleration rate will be discussed in Chapter 4.

The computational procedure is shown in Fig.3.2.

4 Boundary Conditions

There are several boundaries which are fitted to the curvilinear co-ordinate system as shown in Fig.3.3. The detail boundary conditions are as follows.

4.1 Free surface boundary conditions

The flow with the free surface remains still as one of the most challenging problems in the field of fluid mechanics. The primary difficulties arise from the nonlinearlity of the free surface boundary conditions.

The free surface location can be calculated to satisfy the kinematic condition which represents that fluid particles of the free surface always remain on it. In the present study, the following Euler-type kinematic

condition is used.

$$h_t + uh_x + vh_y - w = 0 \tag{25}$$

where $h(x, y, t)$ is the wave height and the subscripts represent partial differentiations with respect to the referred variables. The equation(3.25) is discretized by the first order forward scheme for the time integration and the third order upwind scheme for other terms.

On the other hand, the velocity and pressure can be calculated by an equilibrium of stresses on the free surface as follows;

$$\sigma_{ij} n_j = \sigma^*_{ij} n_j \quad , \quad (i, j = 1, 2, 3) \tag{26}$$

$$\sigma_{ij} = -p\delta_{ij} + \frac{1}{Rn}\left(\frac{\partial u_i}{\partial x_j} + \frac{\partial u_j}{\partial x_i}\right) - \overline{u'_i u'_j}$$

where σ_{ij}, σ^*_{ij}, n_j , δ_{ij} and $-\overline{u'_i u'_j}$ are fluid stress tensor, external stress tensor, unit outward normal vector to the free surface, Kronecker delta and Reynolds stress respectively in the Cartesian co-ordinate system.

Assuming no-shearing stress and excluding the surface tension, the equation(3.26) can be rewritten as follows;

$$\sigma_{ij} n_j n_i = P_{at} \tag{27}$$

$$\sigma_{ij} n_j t_i = 0 \tag{28}$$

where t_i is the unit tangential vector to the free surface.

Finally, the following equations can be used as a dynamic free surface boundary condition assuming that the normal component of the viscous and Reynolds stresses are negligibly small.

$$\phi = \frac{h}{Fn^2} \tag{29}$$

$$2u_x n_x + (u_y + v_x) n_y + (u_z + w_x) n_z = 0$$

$$(v_x + u_y) n_x + 2v_y n_y + (v_z + w_y) n_z = 0 \tag{30}$$

$$(w_x + u_z) n_x + (w_y + v_z) n_y + 2w_z n_z = 0$$

where, h, n_x, n_y and n_z are wave height and (x,y,z)-components of the unit outward vector normal to the free surface respectively. Solving equation(3.30), on the free surface the velocity components can be calculated.

The no-shearing stress condition leads a generation of vorticity on the free surface[36]. The axis of the

vorticity is perpendicular to the streamwise direction and the strength of the vorticity is

$$\omega = 2k_s q_s \tag{31}$$

where, k_s and q_s are the curvature of streamline and streamwise velocity on the free surface respectively. Equation(3.31) means that the curvature of the free surface can generate the vorticity if the streamwise velocity is not zero.

A zero-gradient extrapolation for the velocity is commonly used on the free surface because of the simplicity. In the present study, the above two approaches are compared in Chapter 5.

The detail derivation of the free surface boundary condition is explained in Appendix A.

4.2 Other boundary conditions

Body Boundary

In the curvilinear co-ordinate system used in this study, the body surface is located η-constant plane. On the body surface, a no-slip condition is used for the velocity while Neumann-type condition is applied for the pressure. When the no-slip condition is applied on the body surface, the following linear algebraic equations are obtained.

$$\begin{aligned} \phi_\xi \xi_x + \phi_\eta \eta_x + \phi_\zeta \zeta_x &= F \\ \phi_\xi \xi_y + \phi_\eta \eta_y + \phi_\zeta \zeta_y &= G \\ \phi_\xi \xi_z + \phi_\eta \eta_z + \phi_\zeta \zeta_z &= H \end{aligned} \tag{32}$$

where, F, G and H are defined in equation(3.9).

From the above equations, ϕ_η can be obtained.

Finally, the pressure can be calculated on the body surface by the following way.

$$\phi_j = \frac{1}{3}(4\phi_{j+1} - \phi_{j+2} - 2\phi_\eta) \tag{33}$$

On the other hand, it is difficult to treat the intersection of the free surface and solid body because the region is a kind of a singular one[37]. In this study, no-slip condition is used for the velocity and wave elevation is linearly extrapolated using several neighboring points on the free surface which are calculated by the kinematic free surface boundary condition. The pressure in this singular region is obtained by the dynamic free surface boundary condition.

Some discussions concerning numerical treatment of the intersection region will be made in Chapter 4.

Symmetry Plane

In half-C type grid systems used in this study, there are two symmetry planes which are forward center plane and wake center plane. On the symmetry plane, the following symmetric condition is applied by assuming that the flow is symmetric there.

$$v = u_y = w_y = \phi_y = h_y = 0 \tag{34}$$

Inflow Boundary

A uniform velocity and zero wave elevation are applied on inflow boundary as follows;

$$u = U_0$$

$$v = w = \phi = h = 0 \tag{35}$$

Outer boundary

Outer boundaries are made up by side, downstream and bottom boundaries. Sometimes, improper boundary conditions give some numerical troubles such as reflection or oscillation of waves on the outer boundaries[38]. However, a simple zero-gradient extrapolation can be acceptable to investigate the flow near the body because the outer boundary or the grid arrangement around the far field region does not affect so much the flow near the body when the computational domain is large enough.

In the present study, the following simple zero-gradient extrapolation is used on all the outer boundaries.

Side boundary:

$$u_\eta = v_\eta = w_\eta = \phi_\eta = h_\eta = 0 \tag{36}$$

Downstream boundary:

$$u_\xi = v_\xi = w_\xi = \phi_\xi = h_\xi = 0 \tag{37}$$

Bottom boundary:

$$u_\zeta = v_\zeta = w_\zeta = \phi_\zeta = 0 \tag{38}$$

5 Turbulence Model

Turbulence model for the flow with free surface around a ship like body is complicated and not well developed yet. In this study, the turbulence transportation is described by using an algebraic eddy-viscosity

model proposed by Baldwin and Lomax[39] which is widely used in computational fluid dynamics for its simplicity.

The Baldwin-Lomax formulation works with a two-layer algebraic eddy viscosity defined as follows;

$$\nu_t = \begin{cases} (\nu_t)_{inner} & \text{if } n \leq n_{crossover} \\ (\nu_t)_{outer} & \text{if } n > n_{crossover} \end{cases} \tag{39}$$

where n is the normal distance from the wall and $n_{crossover}$ is the smallest value of n at which values from the inner and outer formulas are equal.

In the inner region, the Prandtl-Van Driest formulation is used to compute the kinematic eddy viscosity.

$$(\nu_t)_{inner} = l^2|\omega| \tag{40}$$

where $|\omega|$ is the magnitude of the vorticity and l is computed by using the following formula;

$$l = kn\left[1 - exp\left(\frac{-n^+}{26}\right)\right] \tag{41}$$

$$n^+ = \frac{u_\tau n}{\nu} = \frac{n}{\nu}\sqrt{\frac{\tau_w}{\varrho}} \tag{42}$$

In the above expression k=0.4 is the von Kármán's constant and u_τ and τ_w are frictional velocity and wall shear stress respectively.

In the outer region, the eddy viscosity is computed by using the following formula;

$$(\nu_t)_{outer} = KC_{CP}F_{wake}F_{Kleb} \tag{43}$$

where, K=0.0168 is the Clauser's constant and C_{CP}=1.6 is an additional constant.
F_{wake} in equation(3.43) is computed as follows;

$$F_{wake} = min\begin{cases} n_{max}F_{max} \\ C_1 n_{max}u_{DIF}^2/F_{max} \end{cases} \tag{44}$$

Baldwin-Lomax used C_1=0.25 originally. However, Rentze et al.[40] modified the coefficient to 1.0 to make smooth the eddy-viscosity in the streamwise direction. In this study C_1=1.0 is used. F_{max} is the maximum value of the following function.

$$F(n) = n|\omega|\left[1 - exp\left(\frac{-n^+}{26}\right)\right] \tag{45}$$

while n_{max} is the value of n at which F_{max} is found.
u_{DIF} represents the difference between the maximum and minimum total velocity at a fixed x station.

$$u_{DIF} = (\sqrt{u^2+v^2+w^2})_{max} - (\sqrt{u^2+v^2+w^2})_{min} \tag{46}$$

The second term in equation(3.46) is taken to be zero except wake zone where the exponential term of equation(3.41) is set zero.

F_{Kleb} is the Klebanoff intermittency factor as follow;

$$F_{Kleb}(n) = \left[1 + 5.5\left(\frac{C_{kleb}}{n_{max}}\right)^6\right]^{-1} \tag{47}$$

where, $C_{Kleb} = 0.3$ is the Klebanoff's constant.

Degani and Schiff[41] pointed out that the major difficulty encountered in applying the Baldwin-Lomax turbulence model to bodies with crossflow separation was the evaluation of the n_{max} and in turn, of determining $(\nu_t)_{outer}$. Fig.3.4 shows the typical behaviors of the function of $F(n)$ of equation(3.45) at one station. In case that the separation is not so strong, $F(n)$ has a single peak at n=a(Fig.3.4(a)). Thus, the determination of F_{max}, n_{max} and F_{wake} is straightforward. However, in case of a strong separation region, the overlying vortex structure causes a peak in $F(n)$ at n=b(Fig.3.4(b)). As originally implemented, the computed code searches the peak in $F(n)$ occurring at n=b. The choice of the peak at n=b leads a large value of the eddy-viscosity in outer layer. This result will cause that the primary vortices will be smaller than those observed experimentally. In addition, the secondary separation and secondary vortices will not appear in the computed flow[41]. To eliminate this problem, they introduced the following treatment for the determination of the proper F_{max} and n_{max} in the separation region;

The first peak of $F(n)$ was selected if there are several peaks. On the other hand, if there is no peak, the value of the previous station was used[41].

Sung et al.[42] showed that the modification was useful to improve the predictions of axisymmetric stern flows where the separation was intensive.

According to some experimental and numerical findings, separated re-circulating flows exist on the free surface around a shoulder part of a body above a certain velocity[43-45]. Thus, it may be necessary to modify the original Baldwin-Lomax model like Degani and Schiff as mentioned before. However, some difficulties may occur such that the first peak of $F(n)$ has large value or it is located far away from the body. In those cases, a large value of eddy-viscosity can be obtained. On the other hand, it may occur that several stations do not have the peak.

To avoid such problems, in this study, the following modification is introduced.

If $F(n)$ has single peak within a certain range, which is approximately determined by 120 % of a boundary layer thickness of a two-dimensional flat plate, F_{max} and n_{max} can be selected by the value directly. If there are several peaks within the range, the peak having maximum $F(n)$ is selected. On the other hand, if there is no peak of $F(n)$, the maximum value within the range is used as the F_{max}.

The detail discussions for the above modification will be made by a numerical simulation in Chapter 7.

6 Grid Generation

A grid generation is one of the most important factors in CFD because the numerical solution of partial differential equations requires some discretisztion of the field into a collection of points or elemental volume. The use of a curvilinear co-ordinate system makes possible to simplify the computational domain and to facilitate the implementation of boundary conditions strictly.

The grid system is required to be orthogonal and the grid size should be changed smoothly to avoid a numerical error due to the grid system. However, it is difficult to generate a "good grid" satisfying both orthogonality and smoothness near a complicated-shaped body. In that case, a quasi-orthogonal grid can be used by strict treatment of the boundary condition[46]. Another requirements are clustering and minimum grid spacing. These requirements are necessary where the physical values change rapidly within a small distance.

Two types of method for the generation of grid system are widely used. One is analytic method and the other is algebraic one. The analytic method solves a partial differential equation. The method guarantees non-overlapping and smooth grid. However, it is not so easy to control the grid points as desired. On the other hand, the algebraic method uses an interpolation and a smoothing technique which can easily control the grid points. However, the generated grid is liable to be overlapped.

In this study, a geometrical method[47], which is a kind of the algebraic method, is used to generate C-type grid in horizontal plane. The first step of the geometrical method requires an initial grid which can be made by connection of the grid points on the boundaries. And then the initial grid points are iteratively modified to satisfy the several requirements such as orthogonality, smoothness, clustering, minimum grid spacing and so on.

Fig.3.5 shows one example of the generated grid system on the horizontal plane. The initial grid system(Fig.3.5(a)) is given by the connection of grid points between the inner and outer boundaries. Fig.3.5(b) shows an intermediate stage of the iteration. The grid is still not so smooth. Fig.3.5(c) shows the final satisfactory grid system. The grid lines are smooth and clustered near body.

After the generation of the two-dimensional grid system on the horizontal plane, the whole grid system is obtained by stacking it in the vertical direction. The grid lines should be clustered near the free surface to simulate the vortical flows well. The effect of the grid resolution on the vortical flows will be discussed in Chapter 5.

第4章　数値計算法の検証

1 Introduction

A validation of the computed results is important to simulate the physical phenomena within a certain range of accuracy. The use of an unimproved code may lead misunderstanding of the physical phenomena. Thus, some computed results are compared with the experimental ones to validate the code developed in this study. Four kinds of comparisons are made as follows;

1) Double model flow around a vertical strut having parabolic section(L/B=10.0) at Rn=10^6.

2) Double model flow around a vertical strut having NACA0012 section at Rn=10^6.

3) Free surface flow around a vertical strut having parabolic section(L/B=10.0) at Fn=0.25 and Rn=10^6.

4) Free surface flow around a vertical strut having NACA0012 section at Fn=0.25 and Rn=$4.0 \cdot 10^4$.

The computed results of the double model flows are compared with the experimental ones of two-dimensional flows because it is assumed that the strut has a infinite depth and constant section in depthwise direction.

In addition, the numerical treatment of intersection region between the free surface and solid body are investigated together with the effect of oncoming flow acceleration in the initial stage of the computation.

The struts having the parabolic(L/B=10.0) and NACA0012 sections are called PS10 and NS12 respectively hereafter.

The modified Baldwin-Lomax turbulence model described in Chapter 3 is used for the computations of high Reynolds number flows. It is assumed that the flow is turbulent from x=0.10.

2 Results and Discussions

2.1 Double model flow of PS10

Four different grid cases are used to investigate the effect of a minimum grid spacing near body as shown in Table 4.1. The computed results are compared with the near-wall velocity profile called logarithmic law and frictional resistance by Schönherr line.

Fig.4.1 shows one example of generated grid on the horizontal plane. H-type grid system is used because PS10 is sharp wedge model.

Fig.4.2 shows near wall velocity profiles at three different positions. As shown, a turbulent boundary layer is well realized in every cases. However, the frictional resistances in the coarse grid cases(Cases-A and -B) are a little different while the fine grid case(Case-D) has almost the same value with the Schönherr line(Table 4.2).

These results indicate that the minimum grid spacing is one of the important parameters in numerical simulations.

2.2 Double model flow of NS12

The computed pressure distribution is compared with the experimental data for this model. The experimental data(Rn=$2.7 \cdot 10^6$), which was carried out in the wind tunnel, was given by Riegels[48]. The computational conditions are listed in Table 4.3.

Fig.4.3 shows the comparison with the computed and experimented pressure distributions on the body surface. Although the minimum grid spacing is a little large($\Delta\eta$=0.0001), the overall results agree well with each others except the trailing edge. The discrepancy of the trailing edge may be caused by insufficient grid resolution and difference of Reynolds numbers.

Fig.4.4 shows the computed velocity distribution at x=0.80. As shown, the turbulent boundary layer is well realized in the computation.

2.3 Free surface flow of PS10 and NS12

In the pilot computations for the free surface flows, the computed wave profiles along the body surface are compared with the experimental ones.

Computational conditions for both models are tabulated in Table 4.4.

An experiment was carried out in the circulating water channel(CWC) of Hiroshima University to measure the wave profile of NS12. The length and draft of the strut were $0.15m$ and $0.50m$ respectively. Wave profiles along the body surface were measured by use of an image processing system developed at Hiroshima University[49]. During the measurements, a surfactant was used to remove a surface tension[33]. In case of PS10, the experimental result by Ikehata[50] is compared.

As described in Chapter 3, there is a difficulty in numerical treatment of the intersection of free surface and solid body. The effect of the boundary conditions on the intersection region, which are slip and no-slip condition, is investigated. In case of the slip condition, the vertical component of the velocity is linearly extrapolated using the neighboring points on the free surface while no-slip condition is applied for other components because the free surface moves up- and downward directions before the steady state.

Fig.4.5 shows the comparison of wave profiles for PS10. The computed results agree well with the experimental one. There are no differences in the wave profiles at fully developed stage depending on both slip and no-slip conditions. The reason may be that the grid system near body is fine enough and the velocity close to the body surface is almost zero. In this study, all the computations hereafter are performed by using no-slip condition.

In the present computations, the oncoming flow is linearly accelerated in the initial stage of the computation until $t=T_a$. The effect of acceleration rate of oncoming velocity on bow wave is investigated. Two kinds of acceleration rates are compared. One is a suddern acceleration(T_a=1.0) and the other is a slow acceleration(T_a=5.0).

Fig.4.6 shows time histories of the computed wave elevations at leading edge of NS12 for two different accelerations. In case of the slow acceleration(T_a=5.0), the wave elevation reaches to the steady state after the acceleration while it oscillates in the sudden acceleration case(T_a=1.0). This result explains that the free surface flows around a blunt bow is affected by the acceleration rate of oncoming velocity. Thus, in this study, all the computations for the blunt bows are performed using T_a=5.0.

Fig 4.7 shows comparison of wave profiles for NS12. The computed results are good agree with the experimental result. The computed wave profiles around shoulder part(x=0.30) oscillate slightly. The reason may be that the free surface flow around shoulder part of the blunt model is complicated including strong separated flows called shoulder wave breaking[43-45].

Table 4.1 Computational conditions for double model flows of PS10.

	Case-A	Case-B	Case-C	Case-D
Rn	10^6	10^6	10^6	10^6
Grid numbers				
- ξ-direction(i)	119	119	119	119
- η-direction(j)	45	50	50	50
- ζ-direction(k)	7	7	7	7
Min. grid spacings				
- $\Delta\xi$	0.005	0.005	0.005	0.005
- $\Delta\eta$	0.0002	0.00012	0.00008	0.00004
Computational domains	$-1.2 \leq x \leq 3.0$ $0.0 \leq y \leq 1.5$ $-1.0 \leq z \leq 0.0$			

Table 4.2 Comparison of frictional resistance for PS10 at $Rn=10^6$.

	Case-A	Case-B	Case-C	Case-D	Schönherr
$C_f \times 10^3$	4.78	4.80	4.65	4.46	4.41

Table 4.3 Computational conditions for double model flow of NS12.

Rn	10^6
Grid numbers (i x j x k)	101 x 50 x 7
Min. grid spacings - $\Delta\xi$ - $\Delta\eta$	 0.005 0.0001
Computational domains	$-1.5 \leq x \leq 2.5$ $0.0 \leq y \leq 1.5$ $-1.0 \leq z \leq 0.0$

Table 4.4 : Computational conditions for free surface flows of PS10 and NS12.

	PS10	NS12
Rn	10^6	$4.0 \cdot 10^4$
Fn	0.25	0.25
Grid numbers (i x j x k)	139 x 60 x 15	110 x 50 x 20
Min. grid spacings		
- $\Delta\xi$	0.005	0.005
- $\Delta\eta$	0.0001	0.001
- $\Delta\zeta$	0.001	0.001
Computational domains	$-1.2 \leq x \leq 3.0$ $0.0 \leq y \leq 1.5$ $-1.0 \leq z \leq h_{max}$	$-2.0 \leq x \leq 3.5$ $0.0 \leq y \leq 2.0$ $-1.0 \leq z \leq h_{max}$

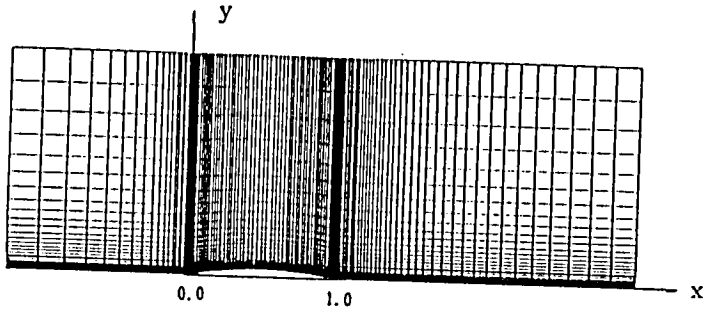

Fig.4.1 Example of Half-H grid on horizontal plane for PS10.

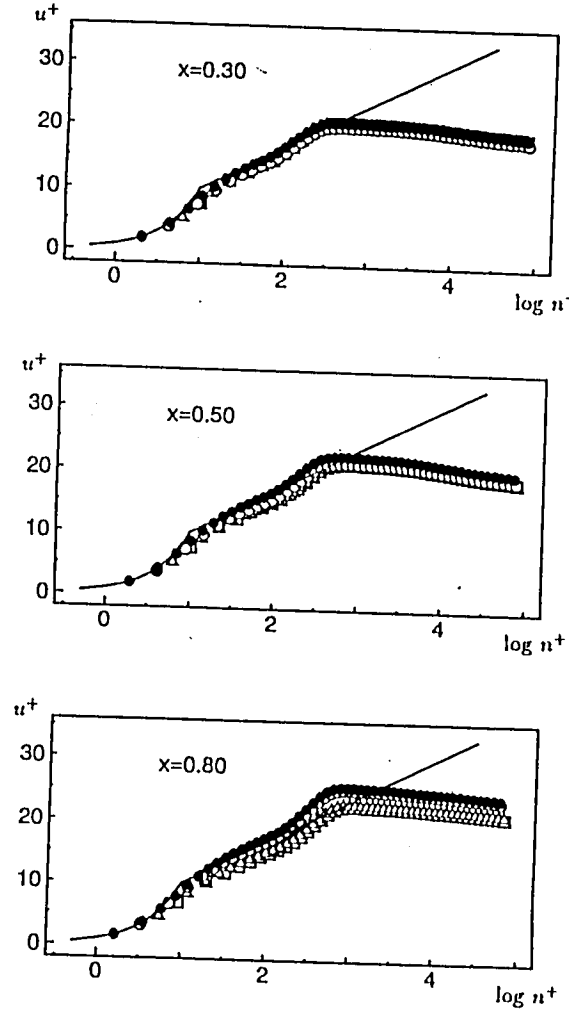

Fig.4.2 Log-plot of velocity profiles of PS10, double model flow, $Rn=1.0 \cdot 10^6$, (—;emperical formula , □;case-A, △;case-B, ○;case-C, ●;case-D).

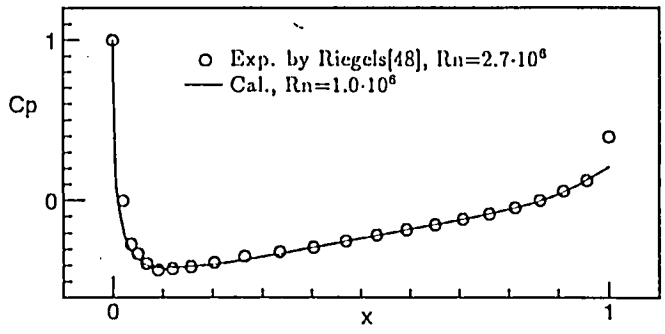

Fig.4.3 Comparison of pressure distributions on body surface of NS12, double model flow.

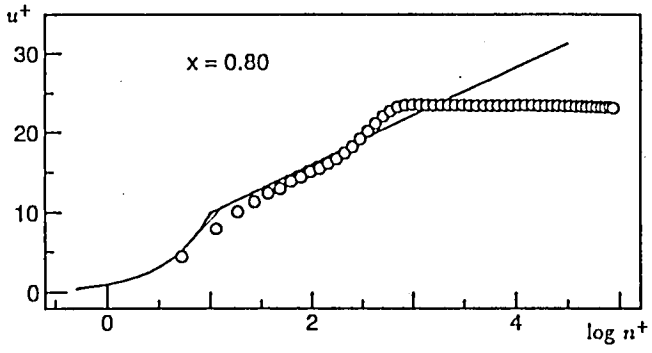

Fig.4.4 Log-plot of velocity profile of NS12, double model flow, Rn=1.0 · 10^6, (—-;emperical formula , o computation).

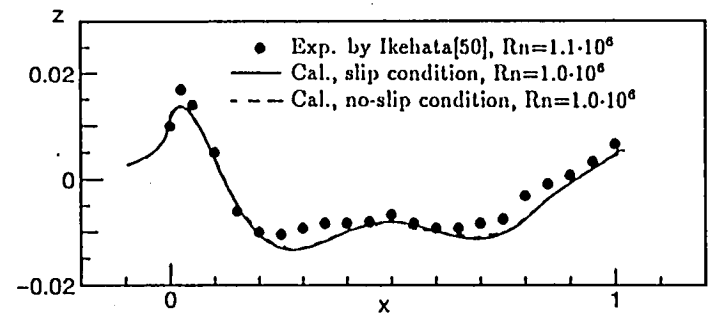

Fig.4.5 Comparison of computed and measured wave profiles on body surface of PS10, Fn=0.25.

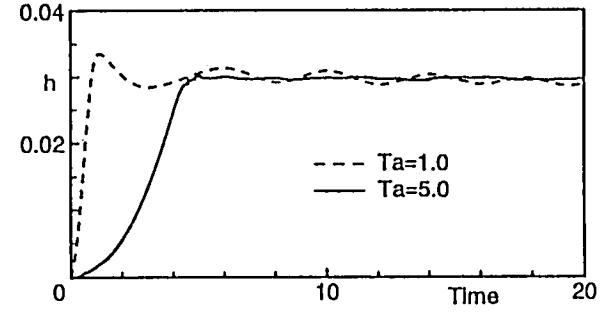

Fig.4.6 Time histories of bow waves by two different acceleration for NS12, Fn=0.25, Rn=4.0 · 10^4.

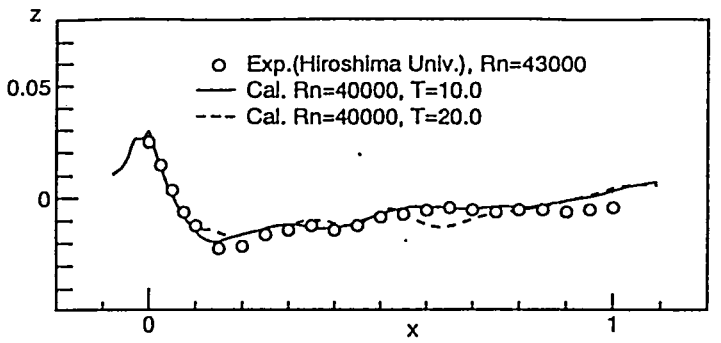

Fig.4.7 Comparison of computed and measured wave profiles on body surface of NS12, Fn=0.25.

第5章　気液界面渦流れ

1 Introduction

Bow breaking wave is one of the most noticeable phenomena in the field of ship hydrodynamics. Not only for a practical ship design but also for a scientific interestings, it is necessary to clarify the mechanism of the breaking waves.

Taneda and Amamoto[2] explained the bow breaking wave as a vortex motion as shown in Fig.2.1. They called it "necklace vortex" to distinguish from the horseshoe vortex which was mainly generated by a boundary layer flow around a body mounted on a plate. They also reported that this necklace vortex was strongly affected by the Froude number while the horseshoe vortex was affected by the Reynolds number[2,3]. Ogiwara et al.[10] reported that the vortical motions were mainly generated by the flow above a stagnation point on the body surface. Takekuma and Eggers[11] explained that the bow wave breaking was characterized by the vortical motions below the free surface. The vortical motions were located just below the free surface where the flow breaked and the region of the vortical motions did not extend widely and the depth was nearly as deep as the wave height. On the other hand, Mori[15] deduced that the formation of the vortex motions was a previous stage of the breaking.

From these situations, it can be considered that the vortex motions are important sources of the breaking

waves.

Moreover, the free surface flows around bow are strongly affected by the bow curvature as shown in Fig.2.14. The large curvature bow(NS08 in Fig.2.14) generates more complicated flow than that of the small one(NS24 in Fig.2.14) although NS24 has much blunter bow. Similar results were obtained by Mori[15] who investigated the curvature effect of the bow using a circular cylinder and an elliptic strut. According to his experimental results, the bow with a larger curvature (elliptic strut) generated more intensive wrinkle, which was a kind of free surface instability, than that generated by the bow with a smaller one(circular cylinder) at the same speed(Fig.2.10).

In this chapter, basic characteristics of the vortical flows beneath the free surface around bow are numerically investigated.

The RaNS and continuity equations are used for the numerical simulations. In the computations of high Reynolds number flows, the modified Baldwin-Lomax turbulence model[41] mentioned in Chapter 3 is used and it is assumed that the turbulent flow starts at x=0.1.

In order to avoid the effect of a draft on the vortical flows around the free surface, it is assumed that the strut has a deep draft and constant section in depthwise direction. Half C-H type grid system is used because the flow is assumed to be symmetric on the centerplane(y=0.0). The no-slip condition is introduced at the intersection region of the free surface and solid body. The oncoming velocity is slowly accelerated until t=5.0 in the computations.

Several computations are performed before the breaking condition. Four different struts having NACA0005, NACA0008, NACA0012 and NACA0024 sections(called NS05, NS08, NS12 and NS24 respectively hereafter) are used to investigate the curvature effect of a bow. The effect of a free surface boundary condition, Froude and Reynols numbers and grid dependency are discussed together.

2 Vortex Generation beneath Free Surface

2.1 Computational conditions

The no-shearing stress condition(equation(3.31)) used in the present study means that the free surface curvature generates a vorticity on the free surface if the streamwise velocity is not zero. However, A zero-gradient extrapolation is often used because of its simplicity.

Liu and Kodama[51] compared the above two approaches in the computations of the free surface flows of Series 60 (Cb=0.60) ship model. They showed that the both treatments gave good agreement with the experimental results.

In this section, those two treatments are compared in the vortical flows point of view. Computations are performed for NS05 and NS12 at Rn=5000 and various Froude numbers.

Computational conditions for the standard case are listed in Table 5.1.

2.2 Discussions

Fig.5.1 shows the computed velocity and vorticity distributions at center plane for two different treatments of the dynamic free surface boundary conditions for NS05 at Fn=0.30. In case of the zero-gradient extrapolation, the computed wave height at the bow is almost the same value as the static head at the stagnation point for inviscid fluid. On the other hand, the introduction of the no-shearing stress condition makes the counter-clockwise vorticity more intensive and the wave height decreases. The maximum vorticity is located just beneath the free surface. This is similar with the experimental results by Takekuma et al.[11] who reported that the vortical motions were located just below the free surface and the region did not extend widely so much and the depth was nearly as deep as the wave height.

Fig.5.2 shows the computed wave profiles along the body surface by the two treatments. The results are almost same except leading edge where the vortical flows are most intensive. In case of the zero-gradient extrapolation, the wave profile around leading edge is sharp. The introduction of the no-shearing stress condition removes the sharp crest of wave profile. This means that the energy accumulated around the wave crest is consumed by the generation of the vorticity.

Fig.5.3 shows the wave contours by the two treatments. The overall patterns are almost same. In both case, the wave systems are developed well.

In case of a lower Froude number flow(Fn=0.25, NS12), however, there are no significant differences between the two results as shown in Figs.5.4 and 5.5.

From these results, it can be concluded that the numerical simulations neglecting the no-shearing stress condition can lead misunderstanding of the phenomena when the vortical flows are intensive although the zero-gradient extrapolation is useful to simulate the propagative wave system.

Fig.5.6 shows the time evolutions of the bow wave formation at center plane during the acceleration for NS05 at Fn=0.30 when the no-shearing stress condition is introduced. At T=3.0, counter-clockwise vorticity(dotted lines) falls appearing on the free surface which has concave curvature. Increasing the upstream velocity, the concave curvature of the free surface becomes larger and the strength of the vorticity increase together. Around T=4.0, a sharp change of the curvature called wave front appears obviously and the peak of the vorticity is located just beneath the free surface around there. However no significant reverse flows are observed. The vorticity exists just beneath the free surface close to the body.

It can be pointed out that the no-shearing stress condition on the free surface plays an important role to produce the vortical motions where the free surface curvature is large. Thus, all the computations are performed taking into account the no-shearing stress condition hereafter.

Fig.5.7 shows the effect of the Froude number for NS05. Increasing the Froude number, the vortical flows become more intensive and the gradient of the wave profile in front of the bow becomes steep. Strong reverse flows appear at a higher Froude number flow(Fn=0.35) around the juncture of the free surface and

strut. The vortical flows do not spread to forward direction. This result can explain that the vortical motions may become more intensive at a much higher Froude number flow and eventually the motions may make the flow unstable.

From these results, it can be concluded that the free surface curvature, especially concave shape, is one of the important sources of the vorticity in front of the bow, which is generated to satisfy the no-shearing stress condition on the free surface. The vorticity induces vortical motions beneath the free surface when the free surface curvature is large.

3 Curvature Effect of Bow

3.1 Computational conditions

The free surface flows around a bow are strongly affected by the curvature of the bow as shown in Fig.2.14. The larger curvature bow(NS08 in Fig.2.14) generates more intensive fluctuations than those in smaller one(NS24 in Fig.2.14). This situation could be also found in Mori[15] as mentioned before.

In this section, the reason of the above situation is numerically investigated. Computations are performed at Rn=5000, 10^4 and 10^5. The computed free surface flows at Rn=10^5 are compared with the experimentally observed results.

Computational conditions for the standard cases are shown in Table 5.2.

3.2 Discussions

Rn=5000 and 10^4

Fig.5.8 shows the vorticity(ω_y) distributions on the free surface on the center plane for NS05, NS08 and NS12 at Fn=0.30 and Rn=5000. Wave height(h) and streamwise velocity(q_s) on the free surface are plotted together. The peaks of the vorticity are located around concave curvature as indicated by dotted arrows. According to the no-shearing stress condition(equation(3.31)), the vorticity on the free surface can be expressed as the product of the free surface curvature and the streamwise velocity. Although the wave front has a larger curvature than that of the concave surface, the vorticity is smaller at the wave front because the streamwise velocity becomes smaller around there. This is the reason why the counter-clockwise vorticity occupies the region in front of the bow. The model with larger curvature bow(NS05) intensifies the concave curvature of the free surface and generates stronger vorticity comparing with other models(NS08 and NS12).

Fig.5.9 shows the vorticity(ω_y) and velocity distributions on the center plane in front of the bows of the three models. The model with larger curvature bow(NS05) generates the most intensive vorticity. The peaks of the vorticity are located beneath the free surface around the wave front for each struts.

Fig.5.10 shows the velocity distributions on the free surface around the bows of the three models. The wave front line of NS05 is clearly observed. Decreasing the curvature of the bow, this line goes away from the body and becomes weak.

From Figs.5.8-5.10, it can be found that the position of wave front is affected by the bow curvature. The distance between bow and wave front of the smaller curvature bow(NS12) is larger than that of the larger curvature bow(NS05). NS08 has about mediate value between NS05 and NS12.

Figs.5.11 and 5.12 show the vorticity distributions beneath the free surface around the bows, where the vorticity is maximum, at Fn=0.30 and Rn=5000 and 10^4 respectively. The distance from the free surface is about 0.005. The vorticity distributed aside from the bow, called a necklace vortex, of NS12 is more intensive than that of NS05, although the strength of the vortical motions of NS12 is less intensive on the center plane in front of the bow. Due to the viscosity of fluid, the vorticity is diffused. On the other hand, even a slight vorticity can form an intensive vortex because of the stretching of vortex tubes, which is mainly caused by a local flow acceleration. The local flow acceleration of NS12 is larger than that of NS05 around the side of the bow. This situation is clearly observed at Rn=10^4(Fig.5.12).

These results are similar to the results by Mori[15] who explained that the necklace vortex of the bow with a smaller curvature(circular cylinder) was more intensive than that of the bow with a larger one(elliptic strut) although the flow on the free surface around the bow of the elliptic strut was more unstable than that of the circular cylinder(Fig.2.10).

Rn=10^5

Fig.5.13 compares the computed and the experimented free surface flows for NS08, NS12 and NS24 at Fn=0.25. The Reynolds numbers for the computation and experiment are 1.0x10^5 and 3.8x10^5 respectively. It is noted that the flow fields around the bows are almost steady both in the experimental and computed results for these cases. The overall computed flow patterns agree well with the experimental results. The wave front lines are clearly shown in both computed and experimented results except NS24. The computed distances between the leading edge(x=0.0) and the wave front on the center plane are about $0.03L$(x=-0.03) and $0.04L$(x=-0.04) for NS08 and NS12 respectively (L: length of the strut). As discussed in low Reynolds numbers cases, the positions of the wave front line are affected by the bow curvature. However, Matsui et al.[12] could not make clear the relation between the bow curvature and the position. The reason may be that it is difficult to measure the position strictly in experiment because the position fluctuates or oscillates in a high Froude number while the position is not clear in a low Froude number.

The comparison of the vorticity(ω_y) and velocity distributions on the center plane in front of the bows for the three models is shown in Fig.5.14. The model with larger curvature bow(NS08) generates the most intensive vorticity which is induced by the free surface curvature as mentioned before. The peaks of the vorticity are located beneath the free surface around the wave front for each models except NS24. In case

of NS24, however, there are no such vortical motions because the free surface is smooth enough. These results can give some explanations to the experimental findings as shown in Fig.2.14; the bow with a larger curvature(NS08) generates more intensive wrinkles than that with the smaller one(NS24).

Fig.5.15 shows the vorticity distributions on the horizontal plane beneath the free surface around the bows at Fn=0.25. The distance from the free surface is about 0.003. The necklace vortex of NS12 is more intensive than that of NS08, although the strength of the vorticity in front of bow of NS12 is smaller. This situation is the same tendency with the low Reynolds number flow as mentioned before. The necklace vortex motions of NS12 at Rn=10^5 are more intensive than those at Rn=5000 and 10^4(Figs.5.11-5.12) although the Froude number is smaller(Fn=0.25 and 0.30 respectively). This can explain that the necklace vortex motions can be affected by the Froude number as well as Reynolds number. In case of NS24, however, there are no such clear necklace vortex. The reason is that the free surface flow of NS24 is premature to generate the vortex motions at this Froude number.

From these results, It can be concluded that the bow shape has strong relation with the free surface curvature, especially concave shape, which is responsible for the vortical flows around the bow.

4 Grid Dependency

4.1 Computational conditions

In CFD, the computed results are strongly influenced by a grid system. The computed results by using an improper grid may lead a misunderstanding of the physical phenomena. Thus, the effect of a grid resolution should be investigated.

In this section, a grid dependency on the vortical flows is investigated for NS12 at Rn=5000 and 10^5. Computational conditions for the standard case are the same as the previous cases as tabulated in Table 5.2.

4.2 Discussions

Fig.5.16 shows the effect of a grid density in vertical direction to the free surface at Fn=0.30 and Rn=5000; minimum grid spacings($\Delta\zeta$) are 0.00075, 0.0015 and 0.003 respectively. The minimum grid spacing and grid density in normal direction to the body surface are kept almost same as shown in Table 5.2. In case of the coarse grid ($\Delta\zeta$=0.003), the vortical motions do not fully develop. On the other hand, the vortical motions develop well for other two cases and almost the same results are obtained for these two cases.

The same investigation is made at a high Reynolds number(Rn=10^5 and Fn=0.25) in Fig.5.17. The minimum grid spacings($\Delta\zeta$) near free surface in vertical direction are 0.0003, 0.0006 and 0.0012 respectively. The minimum grid spacing and grid density in normal direction to the body surface are kept almost same. Although $\Delta\zeta$=0.0010 - 0.0015 are enough in low Reynolds number case as shown in Fig.5.16, in case of a

high Reynold number, however, the size seems to be not enough. Except the case of $\Delta\zeta$=0.0012, the vortical motions develop well and almost the same results are obtained.

Fig.5.18 shows the effect of a grid density in normal direction to the body surface at Fn=0.30 and Rn=5000. The total grid numbers are 91x20x20, 91x45x20 and 91x65x20 respectively in the same computational domain as shown in Table 5.2. The minimum grid spacing in normal direction to the body surface and the grid density in vertical direction are the same for all the cases($\Delta\eta$=0.002 and $\Delta\zeta$=0.0015). Although the minimum grid spacings are kept to be the same, the results are quite different each others. The vortical motions in coarse grid(case(a)) can not be simulated well.

From these results, it can be concluded that the grid density around the free surface is one of the important computational parameters to detect the vortical flows which are induced by the free surface curvature.

Table 5.1 Computational conditions.

Rn	5000
Fn	0.20 - 0.35
Grid numbers (i x j x k)	91 x 45 x 20
Min. grid spacings	
- $\Delta\xi$	0.005
- $\Delta\eta$	0.002
- $\Delta\zeta$	0.0015
Time increment	0.001
Computational domains	$-2.0 \leq x \leq 3.5$ $0.0 \leq y \leq 2.0$ $-1.0 \leq z \leq h_{max}$

Table 5.2 Computational conditions.

	Rn=10^4	Rn=10^5
Grid numbers (i x j x k)	110 x 50 x 20	119 x 60 x 20
Min. grid spacings		
- $\Delta\xi$	0.005	0.005
- $\Delta\eta$	0.001	0.0005
- $\Delta\zeta$	0.001	0.0006
Time increment	0.0005	0.00025
Computational domains	$-2.0 \leq x \leq 3.5$ $0.0 \leq y \leq 2.0$ $-1.0 \leq z \leq h_{max}$	

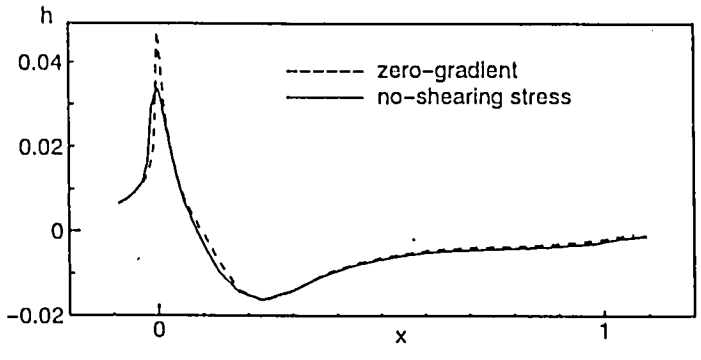

Fig.5.2 Computed wave profiles on body surface; NS05, Fn=0.30, Rn=5000, T=15.0.

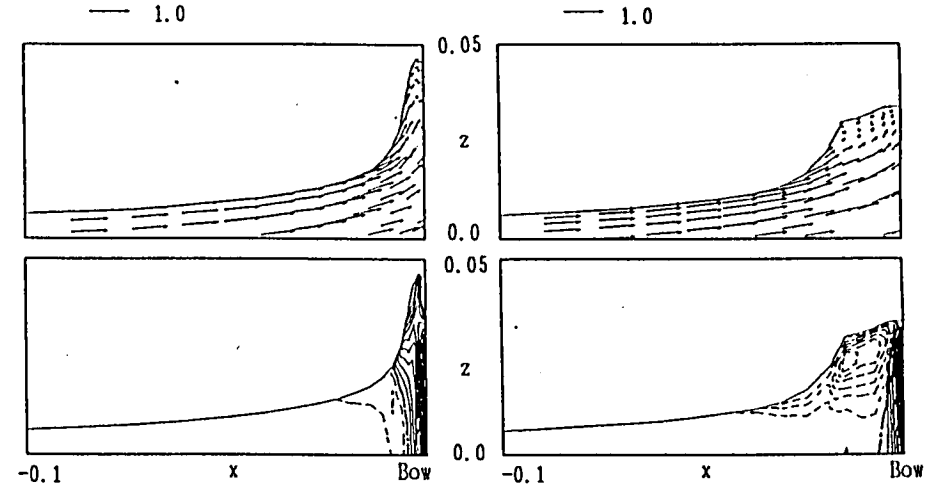

(a) zero-gradient (b) no-shearing stress

Fig.5.1 Computed velocity and vorticity(ω_y) distributions at center plane in front of bow: effect of dynamic free surface boundary condition; NS05, Fn=0.30, Rn=5000, T=15.0 (contour interval=10.0).

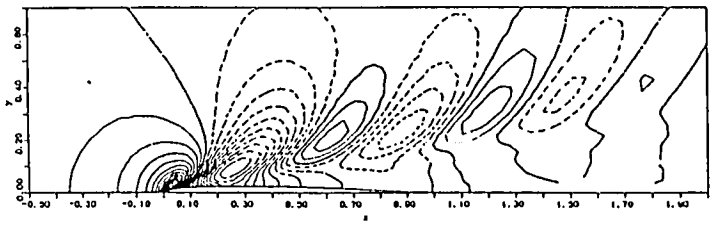

(a) zero-gradient

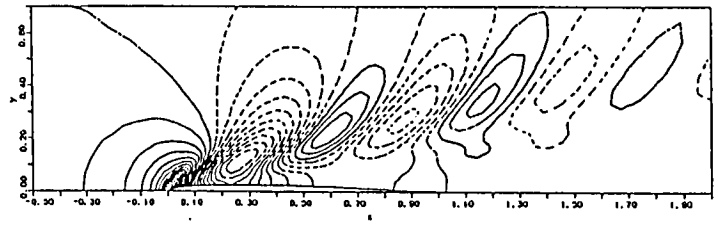

(b) no-shearing stress

Fig.5.3 Computed wave contours; NS05, Fn=0.30, Rn=5000, T=15.0 (contour interval=0.002).

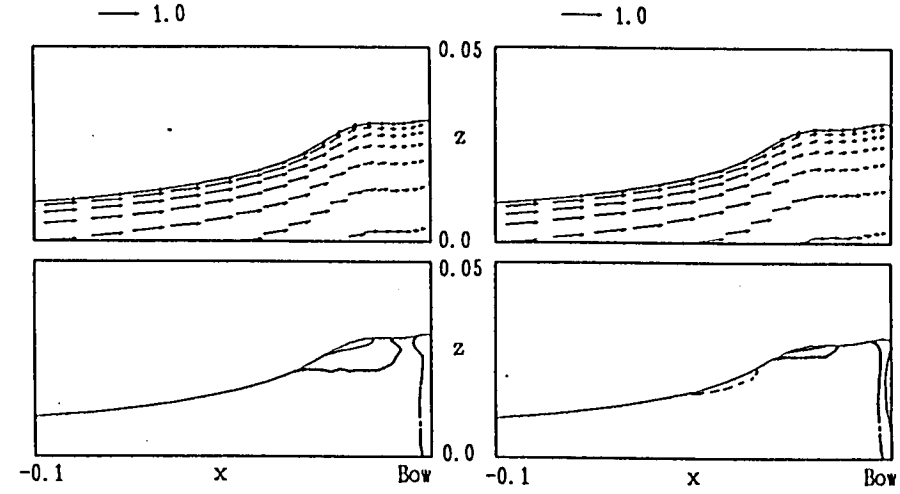

(a) zero-gradient

(b) no-shearing stress

Fig.5.4 Computed velocity and vorticity(ω_y) distributions at center plane in front of bow: effect of dynamic free surface boundary condition; NS12, Fn=0.25, Rn=5000, T=15.0 (contour interval=10.0).

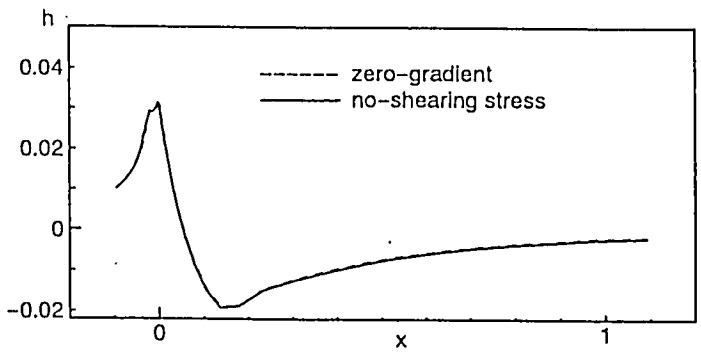

Fig.5.5 Computed wave profiles on body surface; NS12, Fn=0.25, Rn=5000, T=15.0.

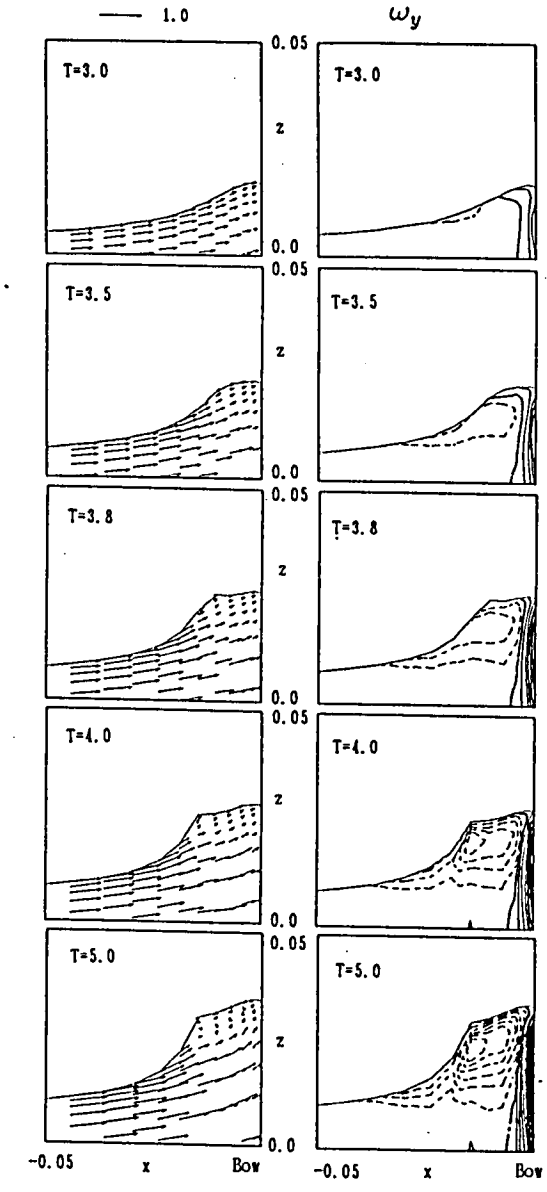

Fig.5.6 Time evolutions of bow wave formation at center plane in front of bow; NS05, Fn=0.30, Rn=5000 (contour interval=10.0).

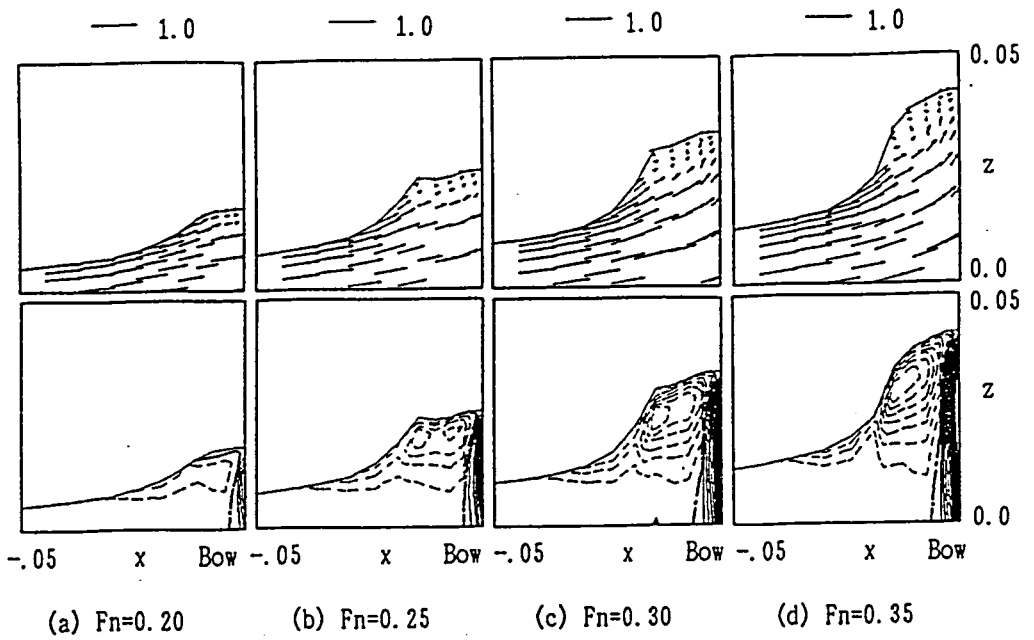

Fig.5.7 Computed velocity and vorticity(ω_y) distributions at center plane in front of bow: effect of Froude number; NS05, Rn=5000, T=15.0 (contour interval=10.0).

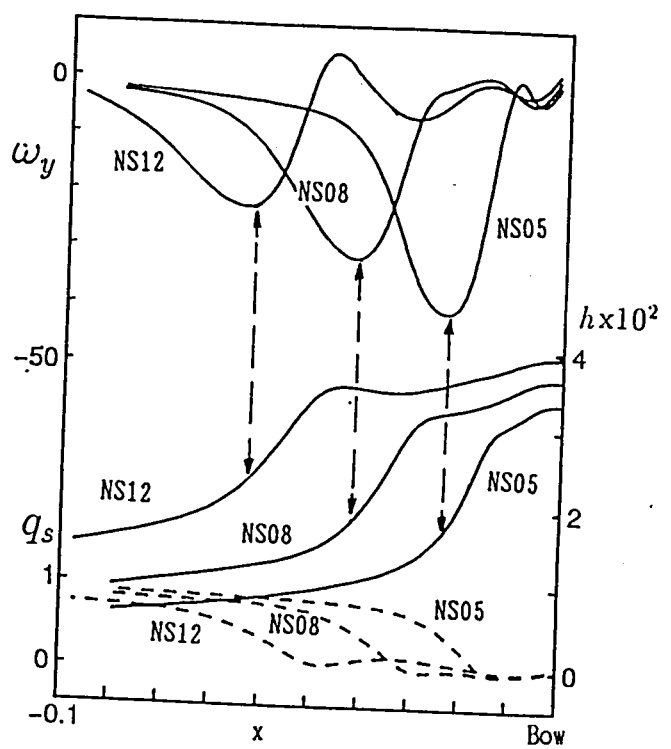

Fig.5.8 Comparison of vorticity(ω_y), wave profile(h) and streamwise velocity(q_s) on the free surface at center plane in front of bow; NS05, NS08 and NS12, Fn=0.30, Rn=5000, T=15.0.

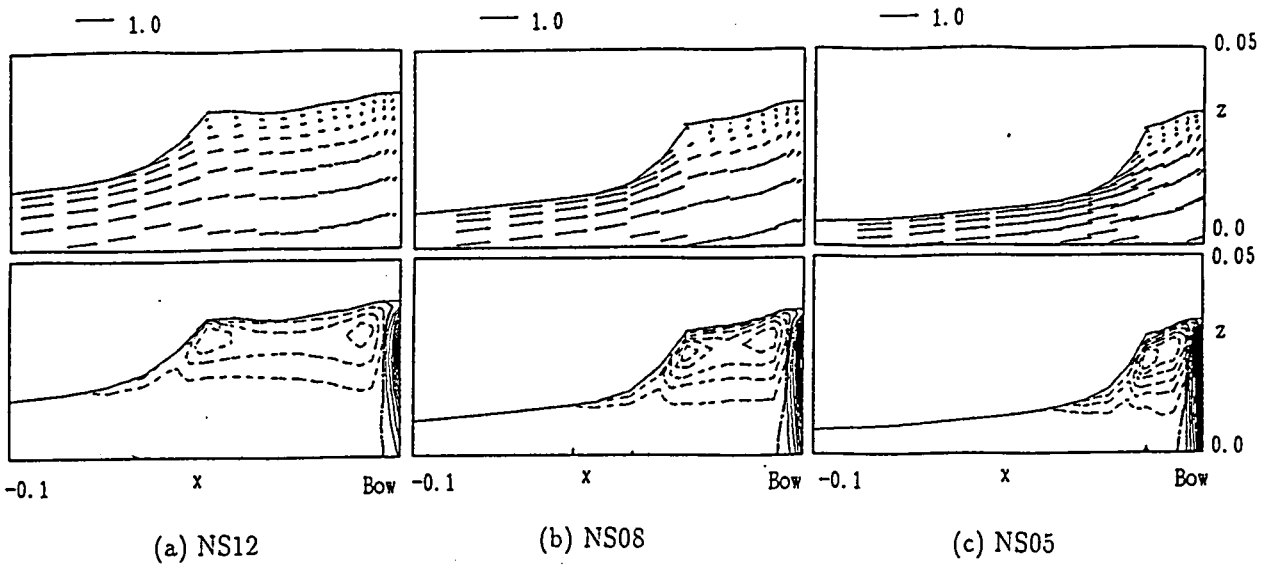

Fig.5.9 Computed velocity and vorticity(ω_y) distributions at center plane in front of bow: effect of bow curvature; NS05, NS08 and NS12, Fn=0.30, Rn=5000, T=15.0 (contour interval=10.0).

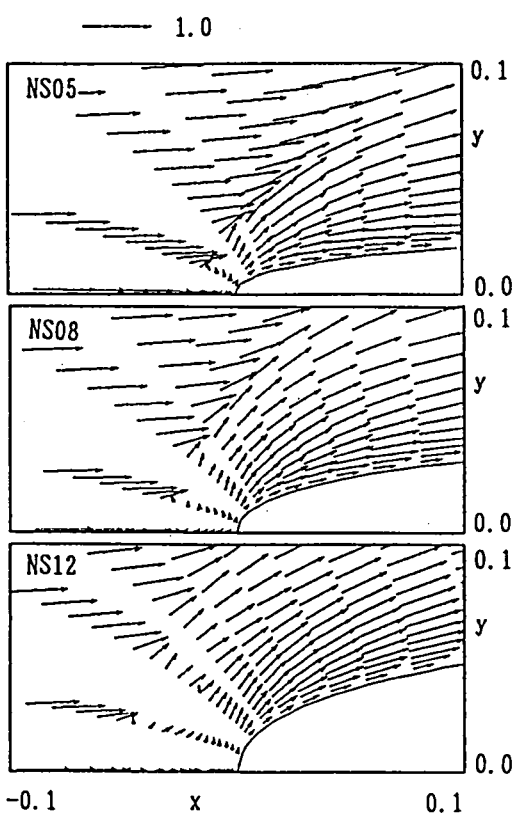

Fig.5.10 Computed velocity distributions on the free surfcae: effect of bow curvature; NS05, NS08 and NS12, Fn=0.30, Rn=5000, T=15.0.

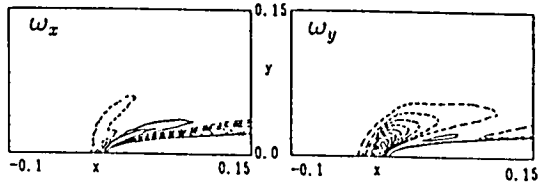

(a) NS05

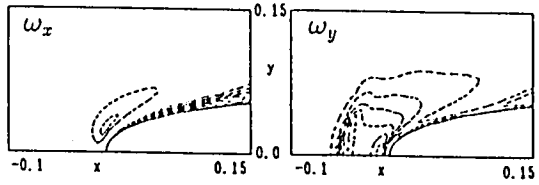

(b) NS12

Fig.5.11 Vorticity(ω_x and ω_y) distributions beneath free surface: effect of bow curvature; NS05 and NS12, Fn=0.30, Rn=5000, T=15.0 (contour interval=5.0).

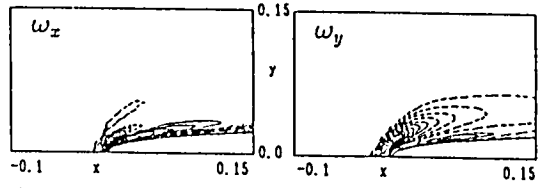

(a) NS05

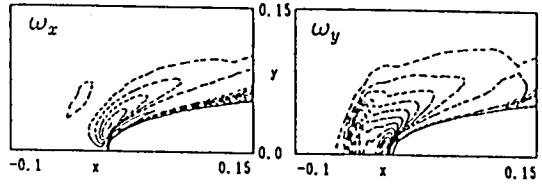

(b) NS12

Fig.5.12 Vorticity(ω_x and ω_y) distributions beneath free surface: effect of bow curvature; NS05 and NS12, Fn=0.30, Rn=10^4, T=15.0 (contour interval=5.0).

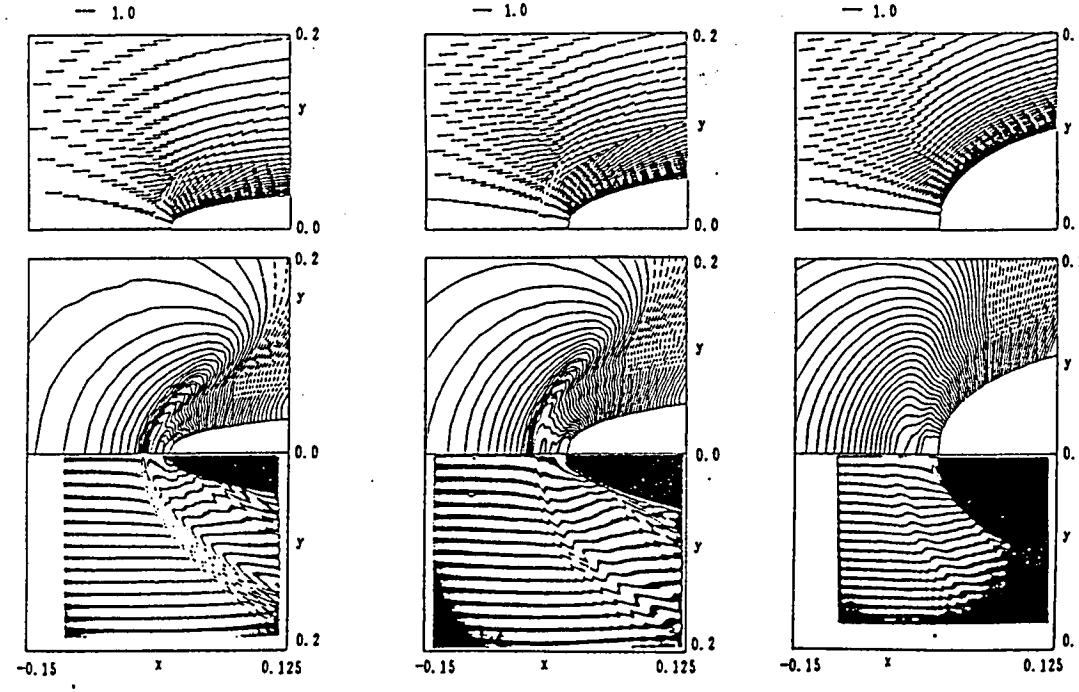

(a) NS08 (b) NS12 (c) NS24

Fig.5.13 Comparison of computed and experimented free surface flows; NS08, NS12 and NS24, Fn=0.25, (above; computed, Rn=$1.0 \cdot 10^5$, down; experimented, Rn=$3.9 \cdot 10^5$).

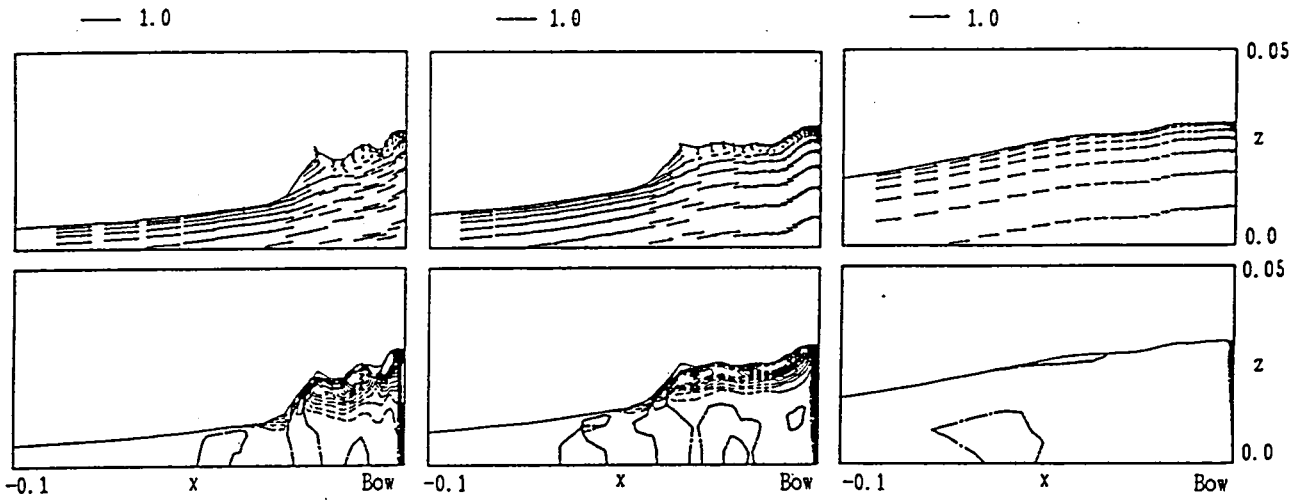

(a) NS08 (b) NS12 (c) NS24

Fig.5.14 Computed velocity and vorticity(ω_y) distributions at center plane in front of bows: effect of bow curvature; NS08, NS12 and NS24, Fn=0.25, Rn=1.0·10^5, T=15.0 (contour interval=10.0).

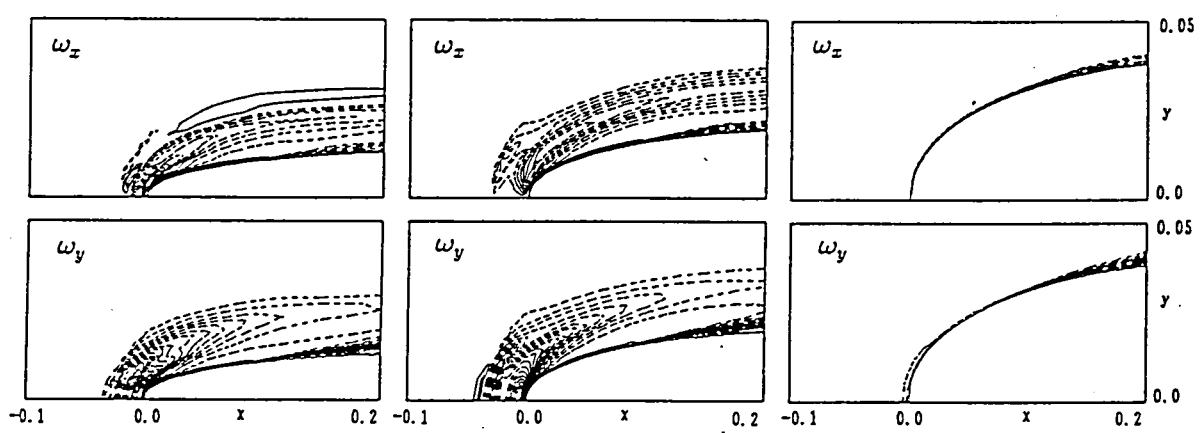

(a) NS08 (b) NS12 (c) NS24

Fig.5.15 Vorticity(ω_x and ω_y) distributions beneath free surface: effect of bow curvature; NS08, NS12 and NS24, Fn=0.30, Rn=10^5, T=15.0 (contour interval=5.0).

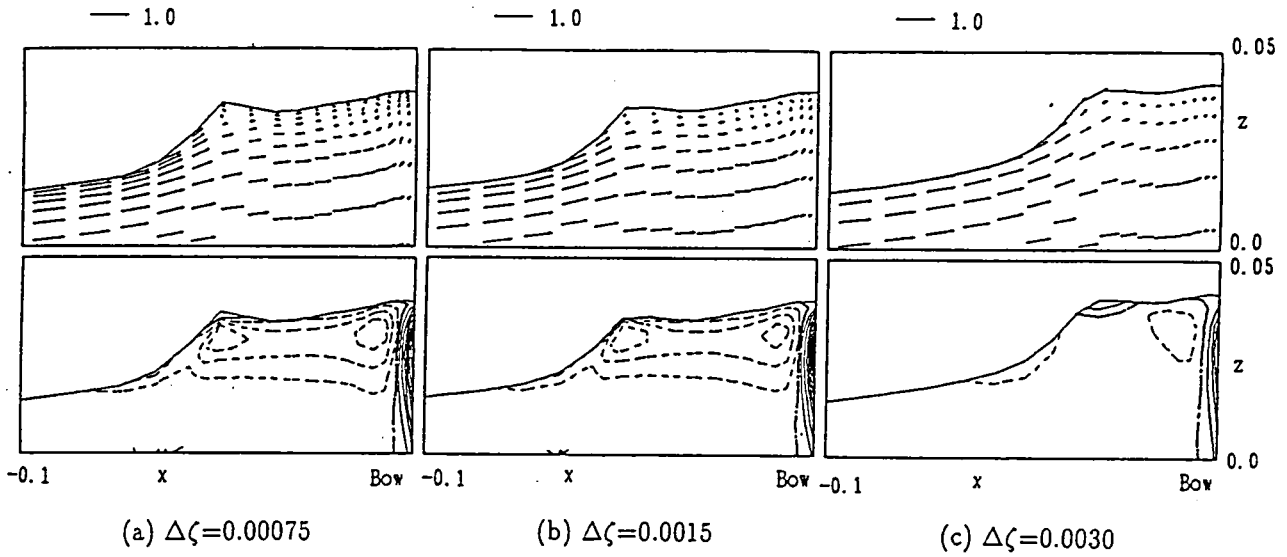

Fig.5.16 Grid dependency of the vortical flows at center plane: effect of $\Delta\zeta$;
NS12, Fn=0.30, Rn=5000, T=15.0 (contour interval=10.0).

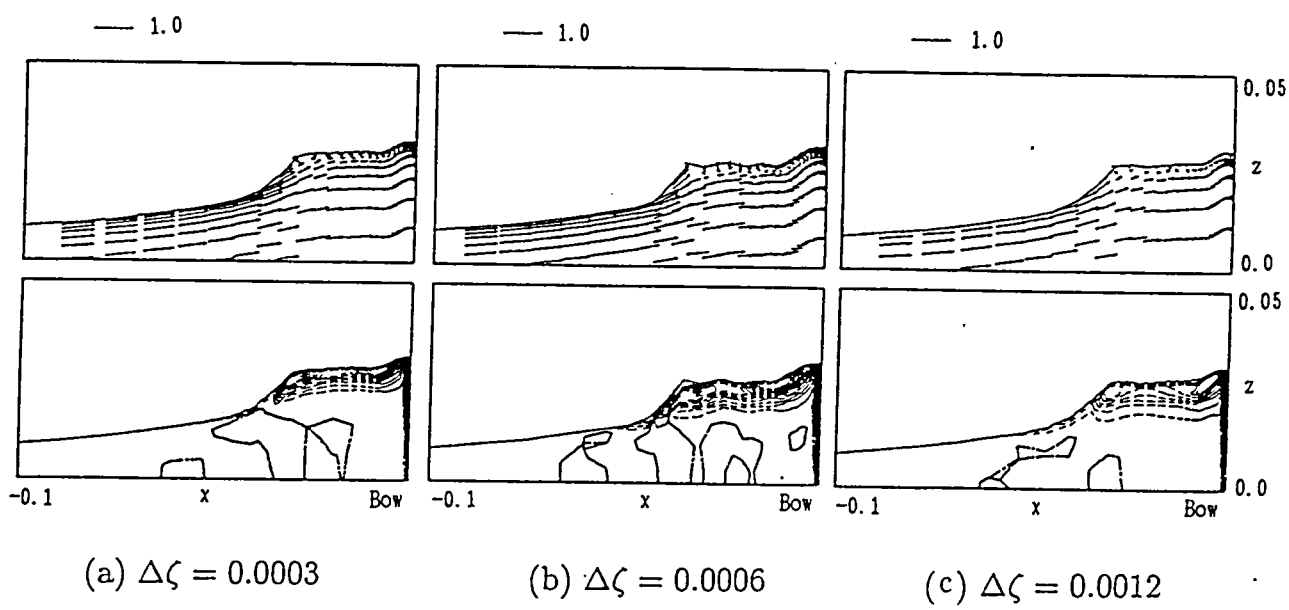

Fig.5.17 Grid dependency of the vortical flows at center plane: effect of $\Delta\zeta$;
NS12, Fn=0.25, Rn=10^5, T=15.0 (contour interval=10.0).

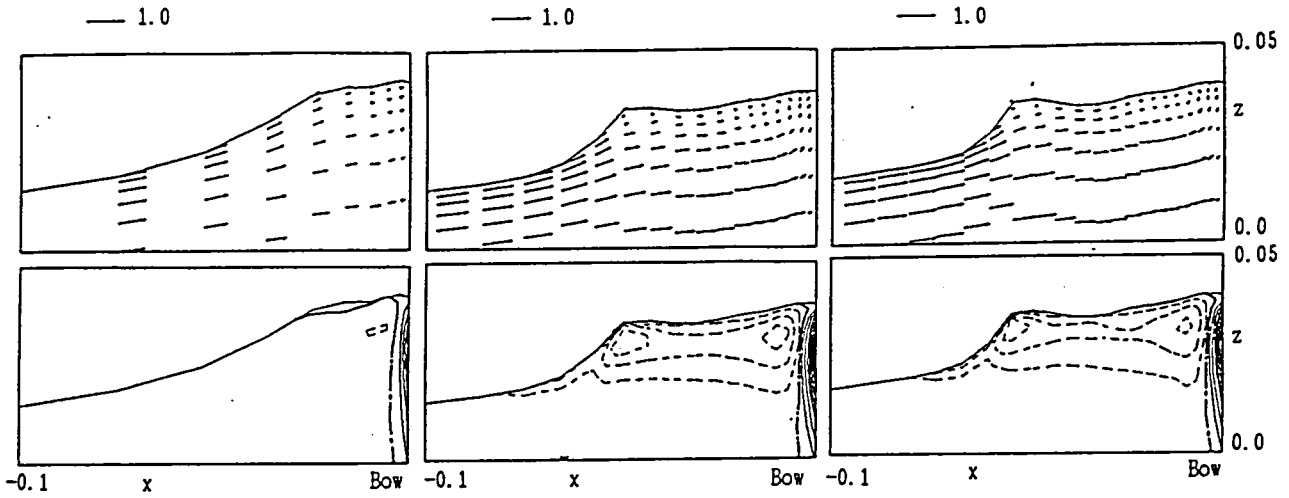

(a) 91 x 20 x 20 grid. (b) 91 x 45 x 20 grid. (c) 91 x 65 x 20 grid.

Fig.5.18 Grid dependency of the vortical flows at center plane: effect of grid density in normal direction to the body surface ; NS12, Fn=0.30, Rn=5000, T=15.0 (contour interval=10.0).

第6章 Sub-breaking wave

1 Introduction

Free surface flows around a bow develop into the quite complicated stage, called wave breaking, above a critical velocity. Since Baba[1] pointed out its importance in ship design point of view, many investigations have been made to clarify the mechanism. However, the so-called bow breaking wave is not so simple as expressed in a word.

Miyata et al.[19] explained that, at a high Froude number, steep waves generated alongside of the bow were nondispersive and they call them "free-surface shock wave". Their numerical simulation was mainly concerned with a plunging breaker. However, Mori[14,15] proposed "sub-breaking wave" as a free surface turbulence in the previous stage of spilling or plunging breakers. He showed the characteristics of the sub-breaking waves through the measurement of the velocity components around the first wave crest generated by a two-dimensional submerged hydrofoil[14]. His experimental results have shown that when the velocity is less than the critical value, the wave crests look rounded and no symptoms of breakings are present and if the velocity increases a little beyond the critical one, the steady breakers suddenly takes place. The wave amplitude under the sub-breaking becomes smaller comparing with that of just before the sub-breaking while the wave length shorter as if Froude number were smaller. If the oncoming flow is further accelerated,

this intermediate stage is overcome by the breakers such as spilling or overturning. He explained that the sub-breaking waves could be understood as follows; the energy accumulated around the wave crest is spent to generate the turbulent flow. The energy of the main stream is transformed into a turbulent energy which dissipates at the same time. Eventually main stream has velocity defects, i.e. headloss, and the flow remains without any catastrophic breakings.

On the other hand, Lungu and Mori[24,25] simulated two-dimensional sub-breaking waves directly by imposing a disturbance for vertical velocity component while Coleman[26] used a disturbance of pressure on the free surface. The role of these disturbances was a kind of a trigger for the transition to the turbulent flow and it could be assumed as a source that maintains the turbulence on the free surface.

As shown in Fig.2.14, the free surface flows of NS08 and NS12 seem to be quite complicated and turbulent which can be called the sub-breaking wave. In this chapter, basic characteristics of the sub-breaking waves are numerically investigated under the similar condition with the experiments.

Large Eddy Simulation(LES) is performed for the strut having NACA0012 section. The Sub-Grid Scale(SGS) turbulence model[52] is introduced for the simulation. An artificial disturbance is introduced to generate fluctuations on the free surface.

2 Numerical Algorithm

2.1 Governing equations

The following three dimensional incompressible space averaged Navier-Stokes and continuity equations are employed for the present numerical study. These governing equations are expressed as the same forms with the RaNS equations(equation(3.1)) which are time averaged Navier-Stokes equations.

$$u_t + uu_x + vu_y + wu_z = -\phi_x + \frac{1}{Rn}\nabla^2 u + S_x$$

$$v_t + uv_x + vv_y + wv_z = -\phi_y + \frac{1}{Rn}\nabla^2 v + S_y \tag{1}$$

$$w_t + uw_x + vw_y + ww_z = -\phi_z + \frac{1}{Rn}\nabla^2 w + S_z$$

$$u_x + v_y + w_z = 0 \tag{2}$$

$$\phi = p + \frac{z}{Fn^2} - P_{at} + \frac{2}{3}k \tag{3}$$

where u, v and w are the velocity components in (x,y,z)-directions in the Cartesian co-ordinate system as shown in Fig.6.1; x in the uniform flow, y in the lateral and z in the vertical directions respectively. The

origin is located at the leading edge of the strut on the undisturbed free surface. Subscripts represent partial differentiations with respect to the referred variables except S_x, S_y and S_z which are SGS stress components. Fn, Rn, ϕ, p, P_{at} and k are Froude number, Reynolds number, modified pressure, pressure, atmospheric pressure and turbulent energy respectively. All the variables are normalized by a uniform velocity(U_0) and the length of strut(L).

The SGS stress terms can be expressed as follows;

$$S_x = \{\nu_s(u_x + u_x)\}_x + \{\nu_s(u_y + v_x)\}_y + \{\nu_s(u_z + w_x)\}_z$$

$$S_y = \{\nu_s(u_y + v_x)\}_x + \{\nu_s(v_y + v_y)\}_y + \{\nu_s(v_z + w_y)\}_z \tag{4}$$

$$S_z = \{\nu_s(u_z + w_x)\}_x + \{\nu_s(v_z + w_y)\}_y + \{\nu_s(w_z + w_z)\}_z$$

where ν_s represents SGS kinematic eddy viscosity.

This method is supposed to resolve the small-scale unsteady turbulent motions[53]. Thus, it may provide useful information for the understanding of the fundamental features of the free surface turbulent flow called sub-breaking wave.

2.2 SGS turbulence model

Sub-Grid-Scale(SGS) turbulence model by Deardroff-Smagorinky is expressed as follows;

$$\nu_s = (C \cdot f_D \cdot L_s)^2 \cdot \{2u_x^2 + 2v_y^2 + 2w_z^2 + (u_y + v_x)^2 + (v_z + w_y)^2 + (u_z + w_x)^2\}^{1/2} \tag{5}$$

where C=0.1 is the Smagorinky's coefficient. L_s is length scale given by;

$$L_s = \Delta^{1/3} \tag{6}$$

where Δ is a cell volume which can be replaced by the Jacobian in this study.

f_D in equation(6.5) is damping factor as follow;

$$f_D = 1 - exp\left(\frac{-n^+}{26}\right) \tag{7}$$

where n^+ is normal distance from the wall normalized by the wall shear stress.

2.3 Numerical approach

Basic solution algorithm is the same as that mentioned in Chapter 3. Half C-H type grid system is used for the simulation because it is assumed that the flow is symmetric on the center plane(y=0.0).

In the computation at high Reynolds and high Froude numbers, two turbulence models are used together. One is the modified Baldwin-Lomax model(MBL) mentioned in Chapter 3 to simulate the flow in the boundary layer on the body and the other is the SGS model for the sub-breaking wave. The combination of these two models is sketched in Fig.6.2. It is assumed that the eddy-viscosity is smoothly changed in the streamwise direction through the intermediate region(INT) where the eddy-viscosity is calculated by the mean of SGS and MBL.

To reduce an artificial viscosity, α=0.5 which is the combination factor of convective terms in equations(3.23) and (3.24) is used.

One of the important characteristics of the sub-breaking waves is the intensive fluctuations of the free surface such as the turbulent flow in the boundary layer flow on a solid body[14,15]. Some disturbances in the boundary layer developed on a body play a role as a trigger for the transition to the turbulent flow and the shear flow of the boundary layer maintains the turbulence. Although the situation is a little different in case of the free surface flow, there exists a boundary layer on the curved free surface which may induce the free surface turbulence. However, in the direct simulation of the turbulence there are no such a trigger. Although a machine epsilon plays a role as the trigger, it is not so strong to generate the turbulence. Thus, an artificial disturbance is often used to simulate the turbulence directly[24-26,54].

In the present numerical study, the following numerical disturbance is introduced.

$$w_d = \beta \cdot (0.5 \cdot u) \tag{8}$$

where β is a random constant(-1.0 $\leq \beta \leq$ 1.0) and u is the calculated velocity of x-component on the free surface. This disturbance is added on the free surface in the region where the SGS turbulence model is introduced as indicated in Fig.6.2 only for two successive time steps after T=4.0.

All the boundary conditions are the same as those mentioned in Chapter 3.

3 Results and Discussions

3.1 Computational conditions

Computations are performed for the strut having NACA0012 section(called NS12 hereafter) at Fn=0.25 and 0.30 and Rn=10^5. The flow conditions are the same as the experiments as shown in Figs.2.13 and 2.14.

Although a sufficient fine grid system and a small time increment are necessary to simulate the fluctuations directly with the SGS turbulence model, it is hard to use satisfactory computational parameters because of a restriction of available memory size and computing time. To avoid the difficulties, a smaller computational domain is used in the present sub-breaking computations. The computational domain and the conditions are tabulated in Table 6.1.

3.2 Discussions

Fig.6.3 shows the computed and observed flow patterns on the free surface around bow at Fn=0.30. The Reynolds numbers of the computation and the experiment are 1.0x10^5 and 4.6x10^5 respectively. The simulated wave pattern agrees well with the experimented one. The distances between the wave front and the bow(x=0.0) are about 0.05L(x=-0.05) and almost the same for the both. However, the computed wrinkles near bow seem smaller compared with the experimental result. The reason may be that the grid system is still not fine enough to simulate the wrinkles.

Fig.6.4 shows the computed velocity and vorticity(ω_y) distributions on the center plane at T=10.0. Several peaks of the free surface exist. It must be noted that the flow around the bow is still fluctuating. Although there are reverse flows in the bow wave field, they are not followed by overturning wave. The vortical flows exist just beneath the free surface close to the bow.

The characteristics of the turbulence on the free surface are investigated at the six points around bow as shown in Fig.6.5. Time history of velocity components, Reynolds stress components and turbulent energy are compared at the points respectively.

Fig.6.6 shows the time histories of velocity components through T=8.0-9.5 at the six points. Although the initial disturbance is imposed all the domain around the bow including point-A, the fluctuations disappear there. The velocity remains almost constant. Thus it can be mentioned that the flow is stable around point-A. The velocity fluctuates slightly at point-B where the concave curvature of the free surface appears. The fluctuations become intensive at point-C which is just outside of the wave front and the free surface curvature is larger. It can be considered that the instability of the free surface starts there. At point-D, the amplitude of the fluctuations of the velocity components becomes larger and the u-component is less than zero. This result indicates that the free surface flows at point-D is turbulent and reverse flows exist there. The fluctuations become gradually weak at points-E, and -F. At point-E, the u-component is still negative and it is a positive at point-F. The reverse flow on the free surface disappears after the point-E. This result can indicate that the turbulence and the reverse flows exist near the bow and they do not extend widely so much. This is similar with the experimental results by Takekuma et al.[11] who reported that the vortical motions, which were strongly related to the breaking waves, were located just below the free surface and the region did not extend widely so much.

Fig.6.7 shows the distributions of time averaged velocity components in depthwise direction at points-A and-D. The velocity is averaged for 15000 time steps from T=8.0 to 9.5. At point-D, where the flow is fully turbulent, the strong defect of the u-component exists close to the free surface while w-component has small defect. On the other hand, there is no such a velocity defect at point-A where the free surface flow is laminar. The similar results are found in the experimental results by Mori[15] who measured the velocity components in front of a elliptic strut and a circular cylinder under the sub-breaking condition.

Fig.6.8 shows the computed Reynolds stress components at point-D. The cross component($\overline{u'w'}$) is almost

zero on the free surface because the no-shearing stress condition is imposed on the free surface. On the other hand, other components become larger on the free surface. $\overline{w'w'}$ is larger than $\overline{u'u'}$. This means that the free surface mainly fluctuates in vertical direction. However, This result is opposite tendency to the experimental results by Mori[15] who showed that $\overline{u'u'}$ was larger than $\overline{w'w'}$. In that point of view, more studies should be required to make clear the phenomena.

Fig.6.9 shows the turbulent energy profiles in depthwise direction at points-A and -D. At point-A, the turbulent energy is almost zero while, at point-D, it is intensive on the free surface and it abruptly becomes weak at the depth of $0.02L$ from the free surface.

As shown in Fig.2.13, the free surface flow at Fn=0.25 seems to be stable. Computations are performed at the similar condition(Fn=0.25, Rn=10^5) for NS12.

Fig.6.10 shows the computed velocity and vorticity(ω_y) distributions on the center plane at T=10.0. Although the artificial disturbance is imposed at two initial time step of the computation, there are no wrinkles of the free surface at fully developed stage.

Fig.6.11 shows the time histories of velocity components on the free surface on the center plane at x=-0.018. Although the initial disturbance is introduced including the point at T=4.0, no fluctuations appear and the velocities keep almost constant values. These results means that the free surface flow at Fn=0.25 is still premature to maintain the imposed initial disturbance.

From these results it can be pointed out the existence of the free surface turbulence called sub-breaking waves which are generated beyond a certain critical velocity without overturning.

Table 6.1 Computational condition for Large Eddy Simulation of sub-breaking wave.

	Rn=10^5, Fn=0.25, 0.30
Grid numbers	
- ξ-direction(i)	72
- η-direction(j)	60
- ζ-direction(k)	20
Min. grid spacings	
- $\Delta\xi$	0.005
- $\Delta\eta$	0.0005
- $\Delta\zeta$	0.0006
Time increment	0.0001
Computational domains	$-0.7 \leq x \leq 1.5$ $0.0 \leq y \leq 0.7$ $-1.0 \leq z \leq h_{max}$

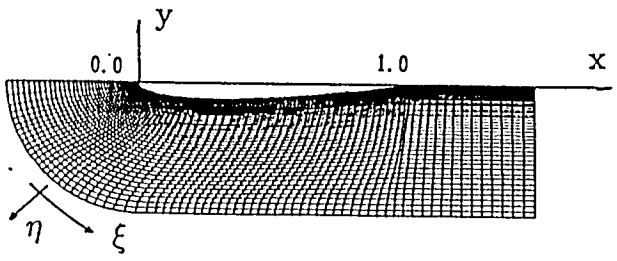

Fig.6.1 Co-ordinate systems and generated grid near body on horizontal plane.

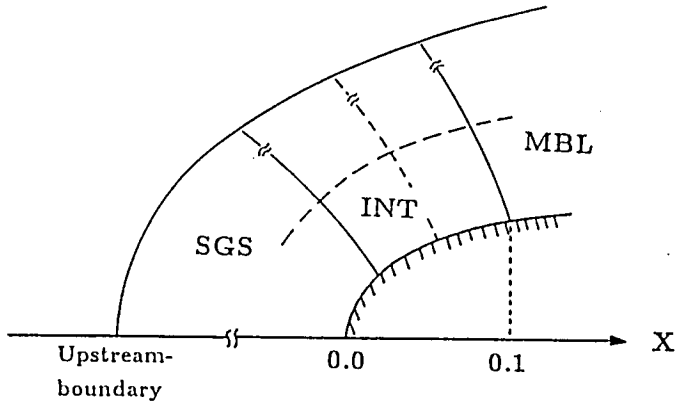

Fig.6.2 Combination of two different turbulence models (SGS; Sub-Grid Scale, MBL; Modified Baldwin-Lomax).

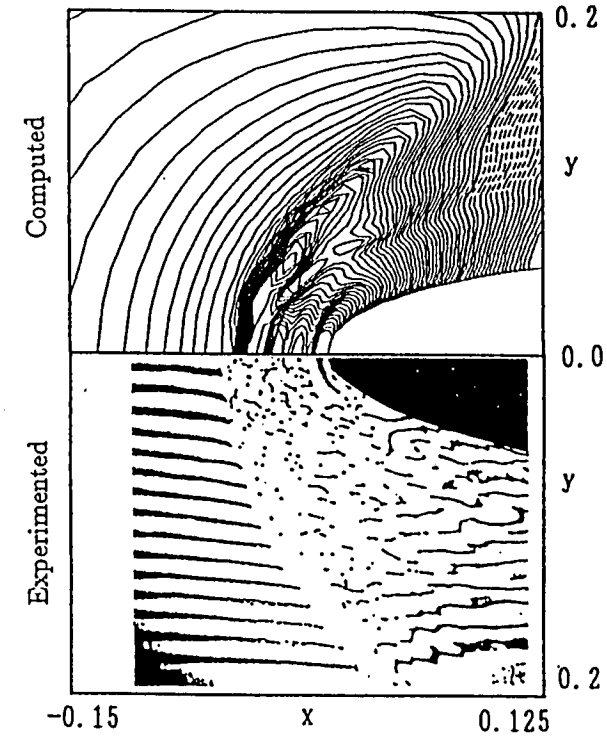

Fig.6.3 Comparison of computed and experimented free surface flows; NS12, Fn=0.30
(upper; computed, Rn=1.0·10^5, down; experimented, Rn=4.6·10^5).

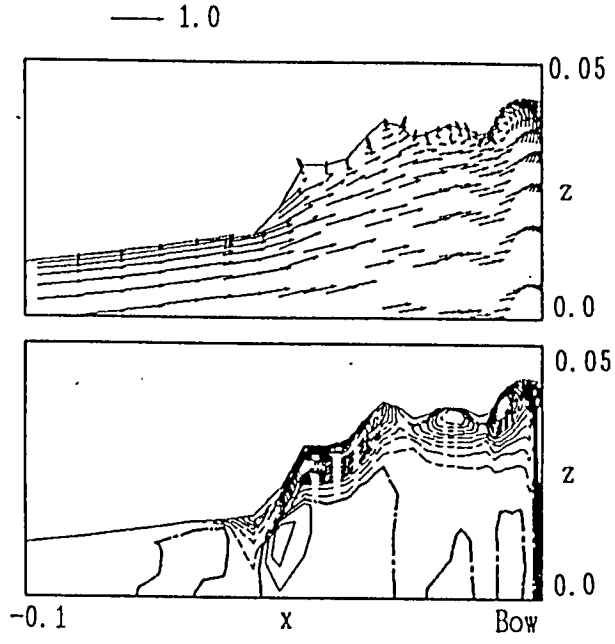

Fig.6.4 Computed velocity and vorticity(ω_y) distributions at center plane in front of bow; NS12, Fn=0.30, Rn=1.0·10^5, T=10.0 (contour interval=10.0).

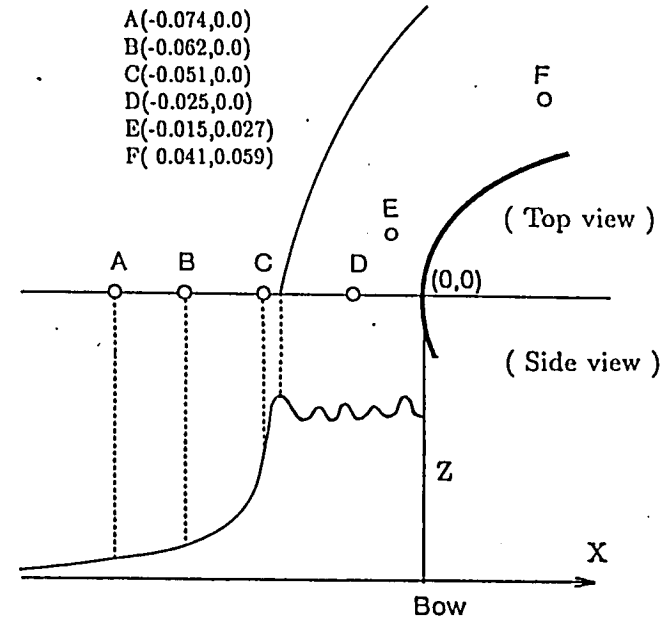

Fig.6.5 Schematic view of bow wave and the definition of six points for investigation of turbulent quantities.

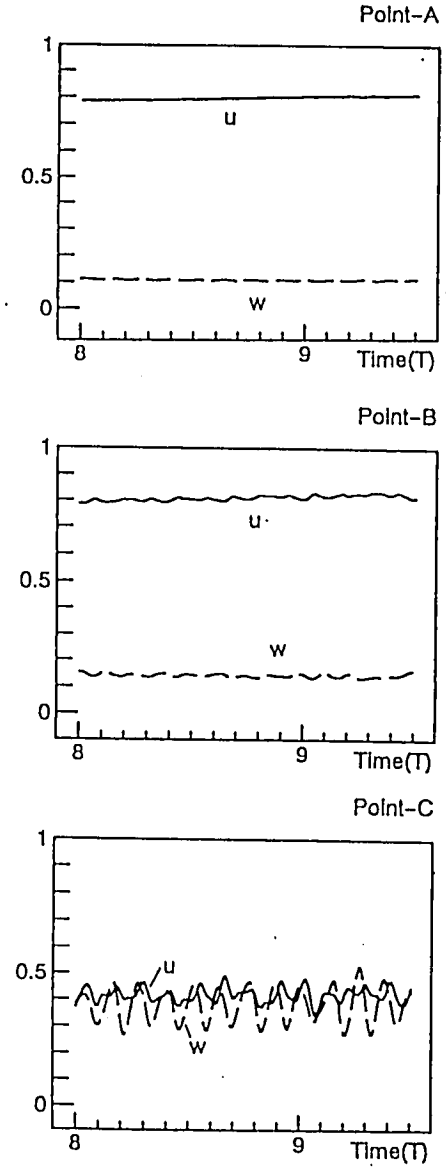

Fig.6.6 Computed time histories of velocity components at six points; Fn=0.30, Rn=1.0·10^5.

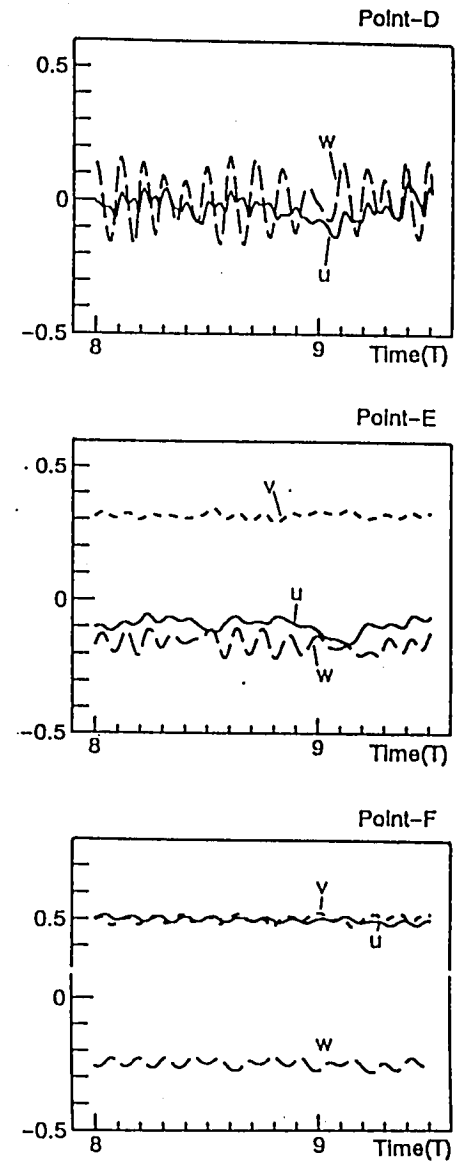

Fig.6.6 (continued)

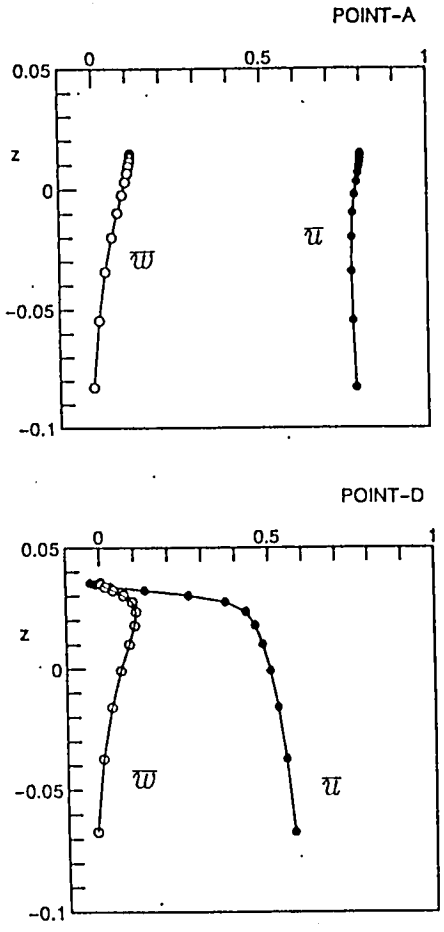

Fig.6.7 Computed mean velocity distributions at points-A and -D;
NS12, Fn=0.30, Rn=1.0·10^5.

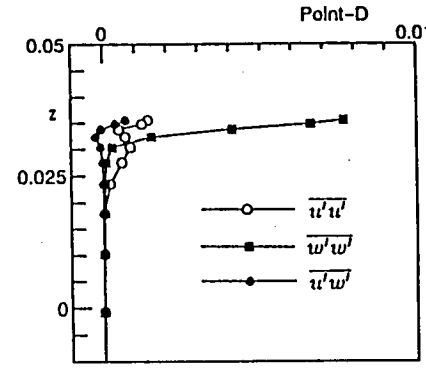

Fig.6.8 Computed Reynolds stress distributions at point-D;
NS12, Fn=0.30, Rn=1.0·10^5.

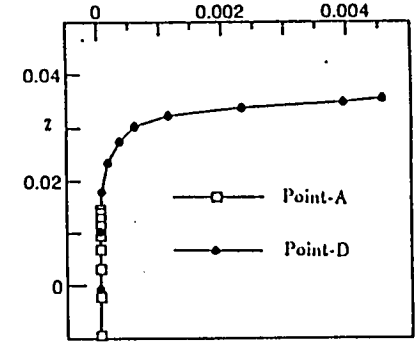

Fig.6.9 Computed turbulent energy distributions at points-A and -D;
NS12, Fn=0.30, Rn=1.0·10^5.

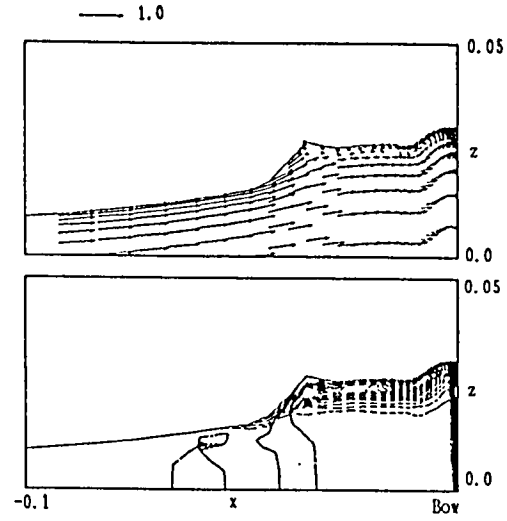

Fig.6.10 Computed velocity and vorticity(ω_y) distributions at center plane in front of bows; NS12, Fn=0.25, Rn=1.0·10^5, T=10.0 (contour interval=10.0).

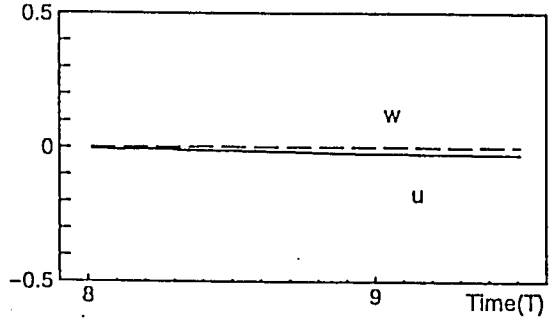

Fig.6.11 Computed time histories of velocity components at a point (x=-0.018, y=0.0) on the free surface; NS12, Fn=0.25, Rn=1.0·10^5.

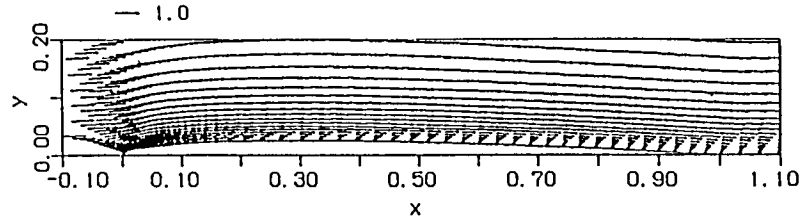

(deep horizontal plane, z=-1.0)

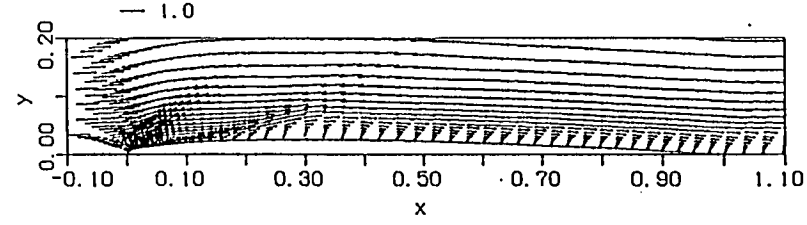

(free surface)

(a) NS05

Fig.7.1 Computed velocity distributions on free surface and deep horizontal plane for NS05 and NS12, Rn=5000, Fn=0.25, T=15.0.

第7章　気液界面での剥離流れ

1 Introduction

Breaking waves around a shoulder part of full entrance hull forms are quite complicated and important phenomena in ship design point of view. Doi[55] and Baba[56] experimentally showed that the viscous boundary layer developed along the hull surface affected the formation of breaking waves around a stern and a shoulder part of the body respectively. Pogozelski et al.[44] carried out a model test of free surface piercing strut having foil section. They showed that the wake flows including bubbles were generated when the Froude number was greater than 0.15 and the flows, they called them "bubbly wake flows", started just down stream of minimum water surface elevation near the body. The position was close to the maximum breadth of the body. Zhang and Stern[45] numerically investigated the free surface flows generated by a surface piercing strut having NACA0024 section. They showed that separated re-circulating flows were generated on the free surface around a shoulder part of the body. They called them "wave-induced separation", which means that the separation is generated by an interaction of the free surface and body. They used the Baldwin-Lomax turbulence model although there are still negative opinions for the application of the turbulence model to the separated flows without modification[41,42].

In this chapter, characteristics of the separated flows on the free surface around the shoulder part of struts are numerically investigated.

The RaNS and continuity equations described in Chapter 3 are used for the numerical simulations. In the computations of high Reynolds number flows, the modification is introduced to the Baldwin-Lomax turbulence model as mentioned in Chapter 3 and it is assumed that the turbulent flow starts at x=0.1. Numerical algorithm and boundary conditions are the same with them explained in Chapter 3. The no-slip condition is introduced at the intersection region of the free surface and solid body. For the simplicity of the problems, it is assumed that the strut has a deep draft and constant section in depthwise direction. Half C-H type grid system is used because the flow is assumed to be symmetric on the centerplane(y=0.0).

Two different struts having NACA0005 and NACA0012 sections are used to investigate a curvature effect of the body.

2 Results and Discussions

2.1 Computational conditions

Computations are performed for two different struts having NACA0005 and NACA0012 sections(called NS05 and NS12 respectively hereafter) at Fn=0.25 and Rn=5000 and 10^5. Computational domains are -2.0 $\leq$ x $\leq$ 4.0, 0.0 $\leq$ y $\leq$ 2.0 and -1.0 $\leq$ z $\leq$ h_{max} for all the computational cases. Computational conditions for the standard cases are listed in Table 7.1.

Table 7.1 : Computational conditions.

	Rn=5000	Rn=10^5
Grid numbers		
- ξ-direction	91	110
- η-direction	45	60
- ζ-direction	20	20
Min. grid spacings		
- $\Delta\xi$	0.005	0.005
- $\Delta\eta$	0.002	0.0005
- $\Delta\zeta$	0.0015	0.0006
Time increment	0.001	0.00025

2.2 Discussions

Typical results of the computed laminar flows are shown in Fig.7.1 which illustrates velocity distributions on the free surface and deep horizontal plane(z=-1.0) for NS05 and NS12 at Rn=5000 and Fn=0.25. There are no separated flows around the shoulder part(x=0.30) on the deep horizontal plane(z=-1.0) for the both models. On the free surface, however, separated flows appear around the shoulder part. The separations of NS12 is more intensive than those of NS05 while its vortical flows around the bow, which are mainly generated by the free surface curvature in front of the bow as mentioned in Chapter 5, is much less than that of NS05 as shown in Fig.7.2.

Fig.7.3 shows the computed velocity distributions on the free surface for two different Froude numbers at Rn=5000 for NS05. In case of Fn=0.30, the separation starts around x=0.30 and the flows become intensive compared with the results of Fn=0.25(Fig.7.1(a)). Increasing the Froude number(Fn=0.35), the position of the separation moves around x=0.40. Fig.7.4 shows the comparison of wave profiles on the body surface. The wave troughs locate around x=0.20 and 0.30 for Fn=0.30 and 0.35 respectively.

From these results, it can be pointed out that the separated flows become intensive at a higher Froude number and the flows start just after the wave trough.

Turbulent flow computations are carried out for NS12 at Rn=10^5 and Fn=0.25. It is assumed that the flow is turbulent from x=0.1. Fig.7.5 shows computed velocity distributions on the free surface and deep horizontal plane(x=-1.0). As shown, on the deep horizontal plane, there are no separated flows. However, on the free surface, separated flows appear around the shoulder(x=0.30) and aft-part(x=0.75) of the body. From Figs.7.1(b) and 7.5, it can be explained that the separated flows at a low Reynolds number are more intensive than those at a high Reynolds number at the same Froude number. The reason is that a boundary layer thickness at a low Reynolds number is thicker than that at higher Reynolds number. Fig.7.6 shows the

vorticity distributions beneath the free surface around the bow. The distance from the free surface is about 0.003 where the vorticity is most intensive. The vorticity distributed aside from the bow, called a necklace vortex, is dissipated away around x=0.20.

From these results it can be explained that the vortical flows or necklace vortex, which are generated beneath the free surface around bow, do not affect so much the separated flows around the shoulder part of the body. The separated flows can be generated by the interaction of a boundary layer and the free surface flows. The separated flows are mainly affected by the local curvature of the body around the shoulder part.

In the present computation, the modified Baldwin-Lomax turbulence model is used for the turbulent flow simulation.

Fig.7.7 shows the behaviors of the $F(n)$ of equation(3.45), which is used to calculate the kinematic eddy-viscosity in outer layer, at x=0.30 for NS12 at Rn=10^5 and Fn=0.25. On the deep horizontal plane(x=-1.0), $F(n)$ has single peak while multi-peaks(two peaks) on the free surface. This is similar situation with Fig.3.4 as pointed out by Degani and Schiff[41]. Fig.7.8 shows the computed kinematic eddy-viscosity distributions at the same station. In case of the original model, the distributions of the eddy-viscosity on the free surface and deep horizontal plane are quite different each other. The value on the free surface by the original model is too large because the second peak of $F(n)$ in Fig.7.7 is selected by the original Baldwin-Lomax model. Introducing the modifications, which means the selection of the first peak in Fig.7.7, it becomes similar to that on the deep horizontal plane and the value seems to be reasonable.

Fig.7.9 shows the velocity distributions on the free surface around the shoulder part(x=0.30). The separated flows by the modified model is slightly intensive than those by the original one. The reason is that the Reynolds stress by the original model may be larger than that of the modified one because the eddy-viscosity by the original model is larger. Thus the velocity defect by the original one becomes larger. By the results, the separated flows of the original one become weak comparing with the modified one as pointed out by Degani and Schiff[41]. However, the wave profiles on the body surface for both treatments are almost same as shown in Fig.7.10. The reason is that the eddy-viscosities close to the body surface, which are not related to the $F(n)$, for both treatments are almost same as shown in Fig.7.8.

From these results it can be concluded that the separated recirculating flows are generated on the free surface around a shoulder part of body due to the interaction of a boundary layer and free surface. The flows start just after the wave trough. The separated flows are not strongly influenced by the vortical flows or necklace vortex which are mainly generated by the free surface curvature in front of the bow.

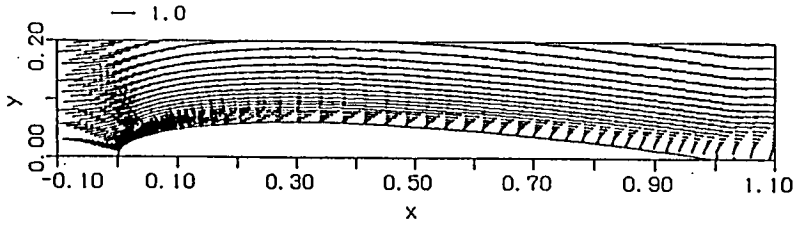

(deep horizontal plane, z=-1.0)

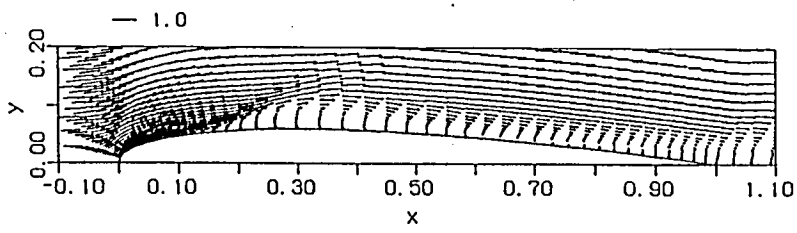

(free surface)

(b) NS12

Fig.7.1 (continued)

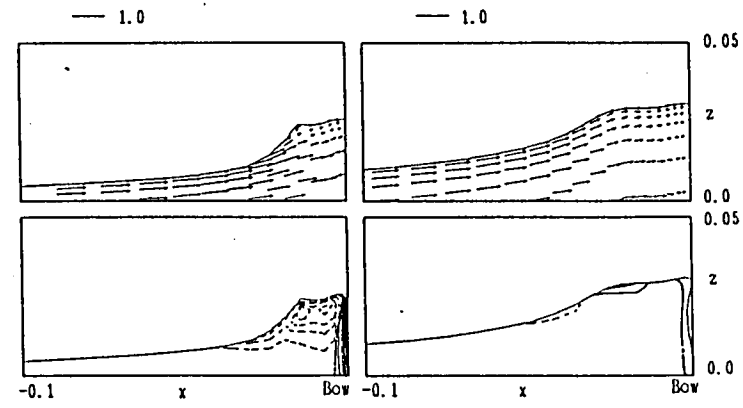

(a) NS05 (b) NS12

Fig.7.2 Computed velocity and vorticity(ω_y) distributions at center plane in fronf of bows of NS05 and NS12, Rn=5000, Fn=0.25, T=15.0.

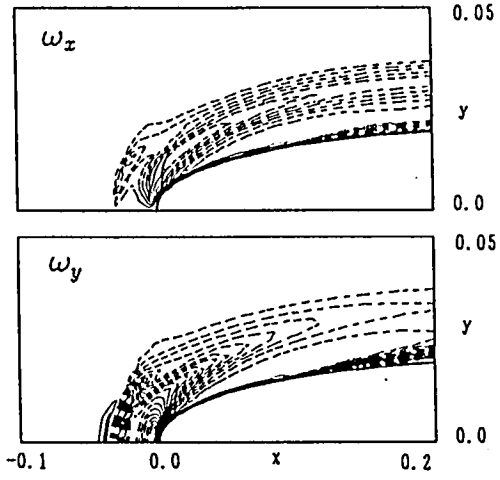

Fig.7.6 Computed vorticity(ω_x and ω_y) distributions beneath free surface, NS12, Rn=10^5, Fn=0.25, T=15.0 (contour interval=5.0).

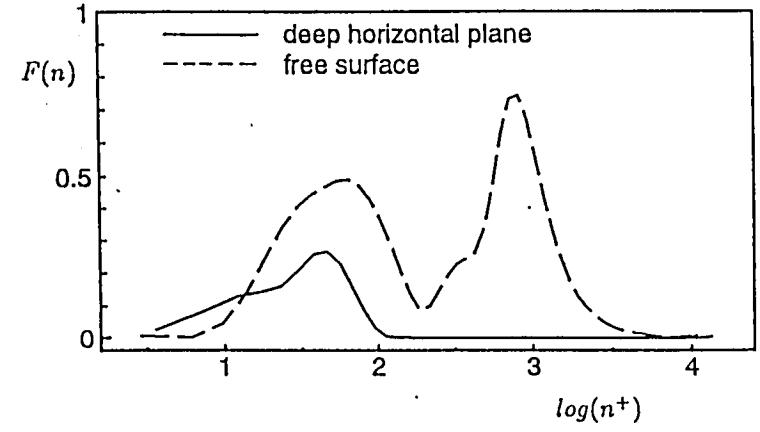

Fig.7.7 Behavior of $F(n)$ at x=0.30, NS12, Rn=10^5, Fn=0.25, T=15.0.

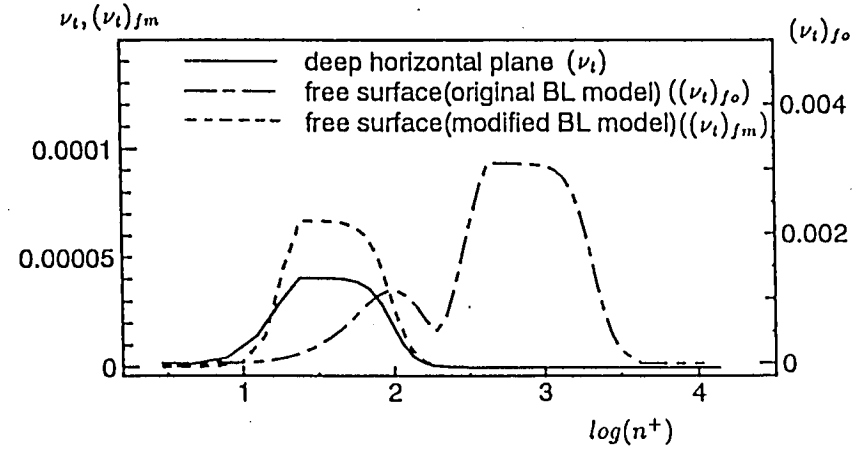

Fig.7.8 Computed eddy-viscosity distributions at x=0.30, NS12, Rn=10^5, Fn=0.25, T=15.0.

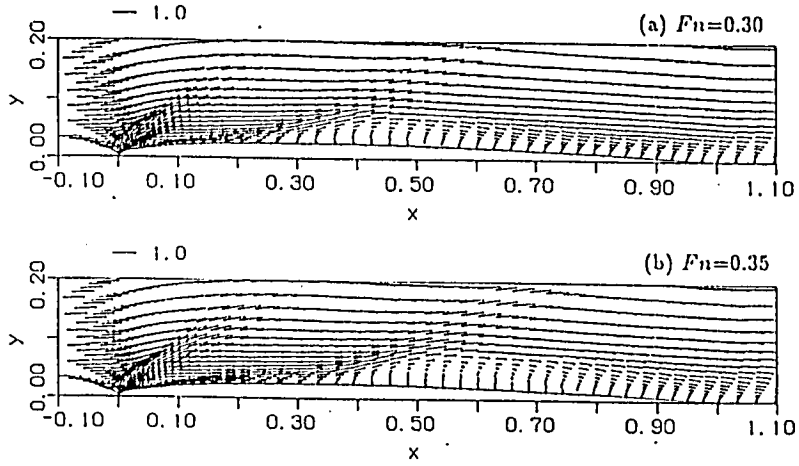

Fig.7.3 Computed velocity distributions on free surface for NS05, Rn=5000, T=15.0.

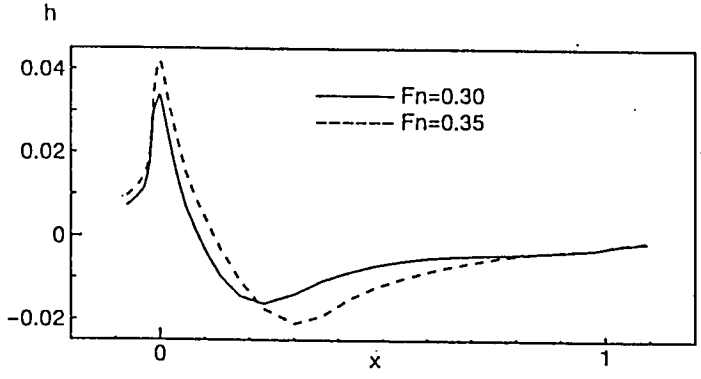

Fig.7.4 Computed wave profiles on body surface, NS05, Rn=5000, T=15.0.

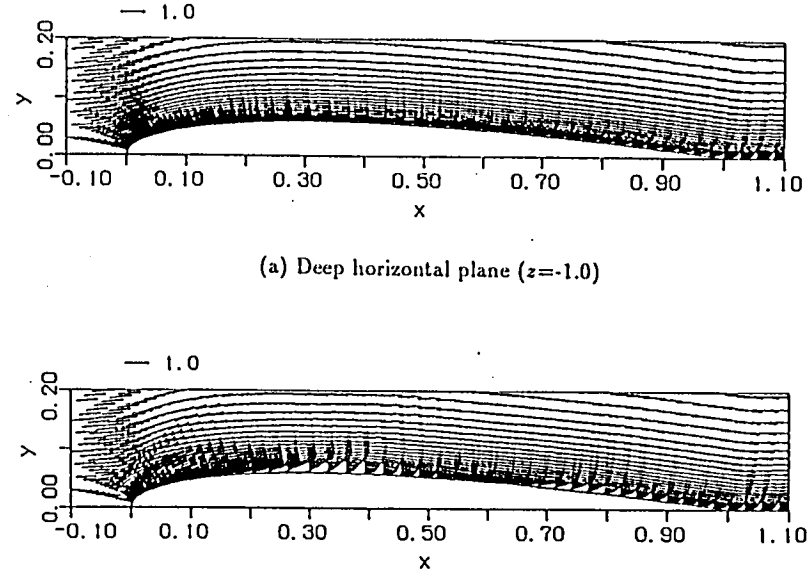

Fig.7.5 Computed velocity distributions on free surface and deep horizontal plane, NS12, Rn=10^5, Fn=0.25, T=15.0.

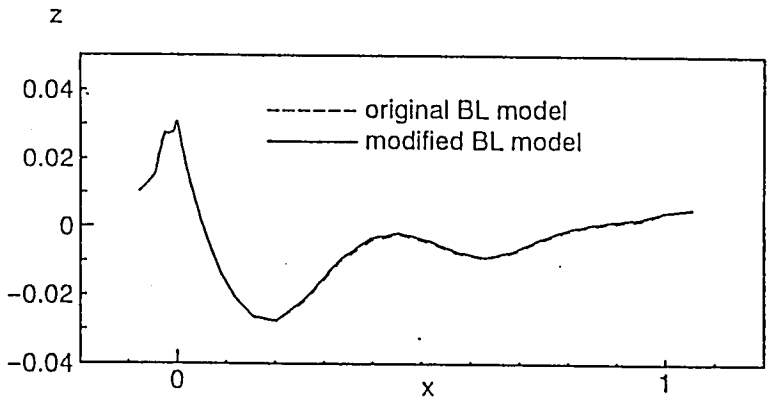

Fig.7.10 Computed wave profiles on body surface, NS12, Rn=10^5, Fn=0.25, T=15.0.

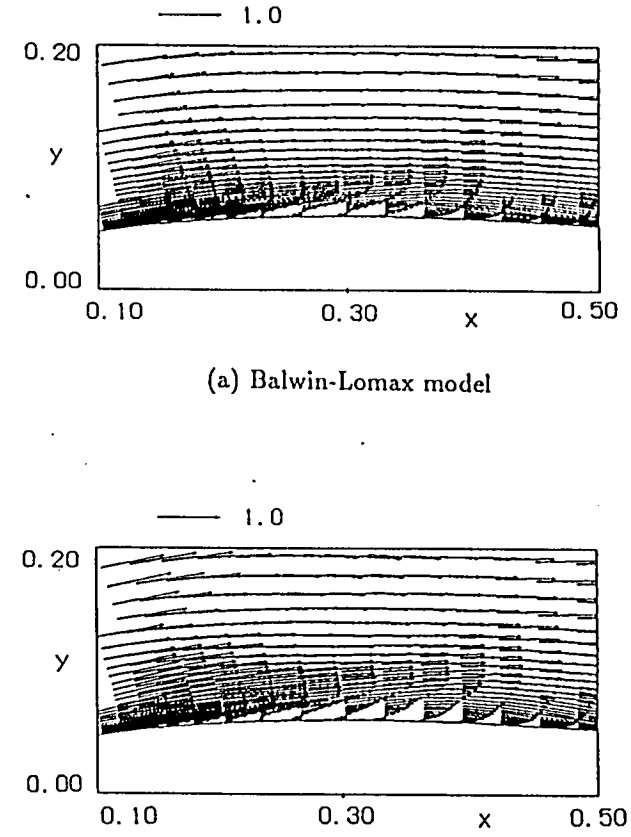

(a) Balwin-Lomax model

(b) Modified Baldwin-Lomax model

Fig.7.9 Computed velocity distributions around shoulder part(x=0.30), NS12, Rn=10^5, Fn=0.25, T=15.0.

参考文献

[1] Baba, E.: *A New Component of Viscous Resistance of Ship*, Journal of the Society of Naval Architects of Japan, Vol.125, pp.23-34, 1969.

[2] Taneda, S. and Amamoto, H.: *The Necklace Vortex of the Ship*, Bulletin of Research Institute for Applied Mechanics, Kyushu Univ., No.31, pp.17-28, 1969 (in Japanese).

[3] Taneda, S: *An Observation of Viscous Flow around Body*, Symposium on Viscous Resistance, The Society of Naval Architects of Japan, pp.35-58, 1973 (in Japanese).

[4] Miyata, H., Kajitani, H., Suzuki, N. and Matsukawa, C.: *Numerical and Experimental Analysis of Nonlinear Bow and Stern Waves of a Two-Dimensional Body (1st Report)*, Journal of the Society of Naval Architects of Japan, Vol.154, pp.48-55, 1983.

[5] Miyata, H., Kajitani, H., Matsukawa, C., Suzuki, N., Kanai, M. and Kuzumi, S.: *Numerical and Experimental Analysis of Nonlinear Bow and Stern Waves of a Two-Dimensional Body (2nd Report)*, Journal of the Society of Naval Architects of Japan, Vol.155, pp.11-17, 1984.

[6] Miyata, H., Baba, N., Kajitani, H., Sato, T. and Shirai, M.: *Numerical and Experimental Analysis of Nonlinear Bow and Stern Waves of a Two-Dimensional Body (3rd Report)-Numerical Simulation Method for Breaking Waves*, Journal of the Society of Naval Architects of Japan, Vol.156, pp.1-12, 1984.

[7] Miyata, H., Kajitani, H., Shirai, M., Sato, T., Kuzumi, S. and Kanai, M.: *Numerical and Experimental Analysis of Nonlinear Bow and Stern Waves of a Two-Dimensional Body (4th Report)-Simulation of Breaking Waves and Experimental Analysis*, Journal of the Society of Naval Architects of Japan, Vol.157, pp.15-33, 1985.

[8] Grosenbaugh, M. A. and Yeung, R. W.: *Nonlinear Bow Flows-An Experimental and Theoretical Investigation*, Proceedings of 17th Symposium on Naval Hydrodynamics, Hague, Netherlands, pp.195-214, 1988.

[9] Kayo, Y. and Takekuma, K.: *On the Free Surface Shear Flow related to Bow Wave-Breaking of Full Ship Models*, Journal of the Society of Naval Architects of Japan, Vol.149, pp.11-20, 1981.

[10] Ogiwara, S., Masuko, A., Sato, R. and Tsutsumi, T.: *Experimental Investigation on Free Surface Flow Related to Bow Wave Breaking*, Journal of the Kansai Society of Naval Architects of Japan, Vol.194, pp.119-131, 1984 (in Japanese).

[11] Takekuma, K. and Eggers, K.: *Effect of Bow Shape on Free Surface Shear Flow*, Proceedings of 15th Symposium on Naval Hydrodynamics, Hamburg, Germany, pp.387-405, 1984.

[12] Matsui, M., Kitazawa, T. and Nagahama, M.: *Observation of Nonlinear Waves around Ship Bow Models*, Journal of the Kansai Society of Naval Architects of Japan, No.190, pp.63-71, 1983 (in Japanese).

[13] Honji, H.: *The Necklace Vortex of the Ship*, Bulletin of Research Institute for Applied Mechanics, Kyushu Univ., No.43, pp.11-17, 1975 (in Japanese).

[14] Mori, K.: *Sub-Breaking Waves and Critical Condition for Their Appearance*, Journal of the Society

of Naval Architects of Japan, Vol.159, pp.1-8, 1986.

[15] Mori, K.: *Necklace Vortex and Bow Wave around Blunt Bodies*, Proceedings of 15th Symposium on Naval Hydrodynamics, Hamburg, Germany, pp.303-317, 1984.

[16] —: Proceedings of SSPA-ITTC Workshop on Ship Boundary Layers, Gothenburg, Sweden, 1981.

[17] —: *Ship Viscous Flow*, Proceedings of the 1990 Workshop, Gothenburg, Sweden, 1991.

[18] —: Proceedings of International Workshop on CFD, Tokyo, Japan, 1994.

[19] Miyata, H., Suzuki, A. and Kajitani, H.: *Numerical Explanation of Nonlinear Nondispersive Waves around Bow*, Proceedings of 3rd International Conference on Numerical Ship Hydrodynamics, Paris, France, pp.37-53, 1981.

[20] Duncan, J. H.: *The Breaking and Non-Breaking Wave Resistance of a Two-Dimensional Hydrofoil*, Journal of Fluid Mechanics, Vol.126, pp.507-520, 1983.

[21] Shin, M. S. and Mori, K.: *On Turbulent Characteristics and Numerical Simulation of Two-Dimensional Sub-Breaking Waves*, Journal of the Society of Naval Architects of Japan, Vol.165, pp.1-7, 1989.

[22] Mori, K. and Shin, M. S.: *Sub-Breaking Wave: Its Characteristics, Appearing Condition and Numerical Simulation*, Proceedings of 16th Symposium on Naval Hydrodynamics, Hague, Netherlands, pp.499-511, 1988.

[23] Hinatsu, M. and Takeshi, H.: *Breaking Waves in front of a Box-Shaped Ship*, Proceedings of 2nd Japan-Korea Joint Workshop on Ship and Marine Hydrodynamics, Osaka, Japan, pp.98-103, 1993.

[24] Lungu, A. and Mori, K.: *Direct Simulation Method for the Breaking Waves*, Proceedings of 2nd Symposium on Nonlinear and Free-Surface Flows, Hiroshima, Japan, pp.40-43, 1993.

[25] Mori, K. and Lungu, A.: *Sub-Breaking Wave and Its Numerical Simulation with Turbulent Characteristics*, Proceedings of 9th International Symposium on Ocean Waves and Floating Bodies, Kyushu, Japan, pp.143-146, 1994.

[26] Coleman, R. M.: *Nonlinear calculation of Breaking and Non-Breaking Waves Behind a Two-Dimensional Hydrofoil*, Proceedings of 16th Symposium on Naval Hydrodynamics, Berkeley, USA, pp.51-62, 1986.

[27] Shin, M. S., Lee, Y.-G., Kim, E.-C. and Yang, S.-I.: *Numerical Simulation of the Nonlinear Free Surface Flow around a Blunt Bow*, Proceedings of 19th Symposium on Naval Hydrodynamics, Seoul, Korea, pp.241-254, 1992.

[28] Park, J. C. and Miyata, H.: *Numerical Simulation of 3D Breaking Wave Motions about an Offshore Structure under a Severe Sea Condition*, Journal of the Society of Naval Architects of Japan, Vol.176, pp.31-42, 1994 (in Japanese).

[29] Patel, V. C., Landweber, L. and Tang, C. J.: *Free-Surface Boundary Layer and the Origin of Bow Vortices*, 2nd International Symposium on Ship Viscous Resistance, Gothenburg, Sweden, pp.23:1-23:13, 1985.

[30] Yeung, R. W. and Ananthakrishnan, J.: *Vortical Flows With and Without a Surface-Piercing Body*, Proceedings of 19th Symposium on Naval Hydrodynamics, Seoul, Korea, pp.183-200, 1992.

[31] Jeong, U.-C. and Doi, Y.: *Numerical Study of Vortical Flows beneath the Free Surface around Struts*, Journal of the Society of Naval Architects of Japan, Vol.178, pp.23-31, 1995.

[32] Jeong, U. C., Doi, Y. and Mori, K.: *Numerical Investigation on the Turbulent and Vortical Motions beneath the Free-Surface around Struts*, Proceedings of 21th Symposium on Naval Hydrodynamics, Trondheim, Norway, pp.——, 1996.

[33] Maruo, H. and Ikehata, H.: *Some Discussions on the Free Surface Flow around the Bow*, Proceedings of 16th Symposium on Naval Hydrodynamics, Berkeley, USA, pp.65-77, 1986.

[34] Welch, J. E., Harlow, F. H., Shabbon, J. P. and Daly, B. J.: *The MAC Method-A Computing Technique for Solving Viscous, Incompressible, Transient Fluid-Flow Problems Involving Free-Surface*, Los Alamos Scientific Laboratory, Report LA-3425, Los Alamos, 1996.

[35] Roache, P. J.: *Computational Fluid Dynamics*, Hermosa Publishers, 1976.

[36] Batchelor, G. K.: *An Introduction to Fluid Dynamics*, Cambridge University Press, pp.364-366, 1970.

[37] Farmer, J., Martinelli, L. and Jameson, A.: *Multigrid Solution of the Euler and Navier-Stokes Equations for a Series 60 Cb=0.6 Ship Hull for Froude Numbers 0.160, 0.220 and 0.316 (Program 1: Navier-Stokes Formulation)*, Proceedings of CFD WORKSHOP TOKYO 1994, Vol.1, pp.56-65, 1994.

[38] Hinatsu, M.: *Numerical Simulation of Unsteady Viscous Nonlinear Waves Using Moving Grid System Fitted on a Free Surface*, Journal of the Kansai Society of Naval Architects of Japan, No.217, pp.1-11, 1992.

[39] Baldwin, B. S. and Lomax, H.: *Thin Layer Approximation and Algebraic Model for Separated Turbulent Flows*, AIAA Paper 78-257, 1978.

[40] Renze, K. J., Buning, P. G. and Rajagopalan, R. G.: *A Comparative Study of Turbulence Models for Overset Grids*, AIAA Paper 92-0437, 1992.

[41] Degani, D. and Schiff, L. B.: *Computation of Turbulent Supersonic Flows around Pointed Bodies Having Crossflow Separation*, Journal of Computational Physics, 66, pp.173-196, 1986.

[42] Sung, C. H., Tsai, J. F., Huang, T. T. and Smith, W. E.: *Effects of Turbulence Models on Axisymmetric Stern Flow Computed by an Incompressible Viscous Flow Solver*, Proceedings of 6th International Conference on Numerical Ship Hydrodynamics, Iowa, USA, pp.387-405, 1993.

[43] Stern, F.: *Effects of Waves on the Boundary Layer of a Surface-Piercing Body*, Journal of Ship Research, Vol.30, No.4, pp.256-274, 1986.

[44] Pogozelski, E., Katz, J., Huang, T.: *Flow Structure around a Surface-Piercing Blunt Body*, Proceedings of 20th Symposium on Naval Hydrodynamics, Santa Barbara, USA, pp.117A-117G, 1994.

[45] Zhang, Z. J. and Stern, F.: *Wave-Induced Separation*, Forum on Advences in Numerical Modeling of Free Surface and Interface Fluid Dynamics, 1995 ASME IMECE, San Francisco, USA, 1995.

[46] Fletcher, C. A. J.: *Computational Techniques for Fluid Dynamics(Second Edition)*, Springer-Verlag, 1991.

[47] Kodama, Y.: *Three Dimensional Grid Generation around a Ship Hull Using the Geometrical Method*,

Journal of the Society of Naval Architects of Japan, Vol.164, pp.1-8, 1988.

[48] Riegels, F. W.:*Airfoil Sections*, Butterworths, London, 1961.

[49] Ninomiya, S., Mori, K., Hosokawa, M.: *Measurements of Wave Height by Visualizing Air-Side Free-Surface and Illuminating the Wetted Surface of Hull through Water*, Journal of the Society of Naval Architects of Japan, Vol.174, pp.129-135, 1993 (in Japanese).

[50] Ikehata, H.: *The Second Order Theory of Wave-Making Resistance*, Journal of the Society of Naval Architects of Japan, Vol.117, pp.—, 1965.

[51] Liu, H. and Kodama, Y.: *Computation of Waves Generated by a Ship Using an NS Solver with Global Conservation*, Journal of the Society of Naval Architects of Japan, Vol.173, pp.1-8, 1993.

[52] Deardorff, J. W.: *A Numerical Study of Three Dimensional Turbulent Channel-Flow at Large Reynolds Numbers*, Journal of Fluid Mechanics, 41, pp.453-480, 1970.

[53] Zhu, M., Miyata, H. and Kajitani, H.: *Finite-Difference Simulation of a Viscous Flow about a Ship of Arbitrary Configuration*, Proceedings of 5th International Conference on Numerical Ship Hydrodynamics, Hiroshima, Japan, pp.83-96, 1989.

[54] Duncan, J. H.: *The Breaking and Non-Breaking Wave Resistance of a Two-Dimensional Hydrofoil*, Journal of Fluid Mechanics, Vol.126, pp.507-520, 1983.

[55] Doi, Y.: *Observation of Stern Wave Generation*, Proceedings of the Continued Workshop on Ship Wave Resistance Computations, Izu Shuzenji, Japan, pp.155-172, 1980.

[56] Baba, E.: *Some Free-Surface Phenomena around Ships to be challenged by Numerical Analysis*, Proceedings of 3rd International Conference on Numerical Ship Hydrodynamics, Paris, pp.9-25, 1981.